

Article

High Strain Rate Properties of Various Forms of Ti6Al4V(ELI) Produced by Direct Metal Laser Sintering

Amos Muiruri ^{1,*}, Maina Maringa ¹ and Willie du Preez ²

¹ Department of Mechanical and Mechatronics Engineering, Central University of Technology, Bloemfontein 9301, Free State, South Africa; mmaringa@cut.ac.za

² Centre for Rapid Prototyping and Manufacturing, Faculty of Engineering, Built Environment and Information Technology, Central University of Technology, Bloemfontein 9301, Free State, South Africa; wdupreez@cut.ac.za

* Correspondence: amos.mwangi.muiruri@gmail.com

Abstract: For analysis of engineering structural materials to withstand harsh environmental conditions, accurate knowledge of properties such as flow stress and failure over conditions of high strain rate and temperature plays an essential role. Such properties of additively manufactured Ti6Al4V(ELI) are not adequately studied. This paper documents an investigation of the high strain rate and temperature properties of different forms of heat-treated Ti6Al4V(ELI) samples produced by the direct metal laser sintering (DMLS). The microstructure and texture of the heat-treated samples were analysed using a scanning electron microscope (SEM) equipped with an electron backscatter diffraction detector for electron backscatter diffraction (EBSD) analysis. The split Hopkinson pressure bar (SHPB) equipment was used to carry out tests at strain rates of 750, 1500 and 2450 s⁻¹, and temperatures of 25, 200 and 500 °C. The heat-treated samples of DMLS Ti6Al4V(ELI) alloys tested here were found to be sensitive to strain rate and temperature. At most strain rates and temperatures, the samples with finer microstructure exhibited higher dynamic strength and lower strain, while the dynamic strength and strain were lower and higher, respectively, for samples with coarse microstructure. The cut surfaces of the samples tested were characterised by a network of well-formed adiabatic shear bands (ASBs) with cracks propagating along them. The thickness of these ASBs varied with the strain rate, temperature, and various alloy forms.

Keywords: direct laser metal sintering; Ti6Al4V(ELI); SHPB; high strain rate; flow stress; fracture strain; adiabatic shear band



Citation: Muiruri, A.; Maringa, M.; du Preez, W. High Strain Rate Properties of Various Forms of Ti6Al4V(ELI) Produced by Direct Metal Laser Sintering. *Appl. Sci.* **2021**, *11*, 8005. <https://doi.org/10.3390/app11178005>

Academic Editor: Marco Sasso

Received: 23 July 2021

Accepted: 22 August 2021

Published: 29 August 2021

Publisher's Note: MDPI stays neutral with regard to jurisdictional claims in published maps and institutional affiliations.



Copyright: © 2021 by the authors. Licensee MDPI, Basel, Switzerland. This article is an open access article distributed under the terms and conditions of the Creative Commons Attribution (CC BY) license (<https://creativecommons.org/licenses/by/4.0/>).

1. Introduction

Direct metal laser sintering (DMLS) is in the additive manufacturing (AM) category of powder bed fusion (PDF) and produces solid parts from 3D CAD models in a layer-by-layer manner by melting metal powders with a focused high energy laser beam. This technology was developed by Electron Optical System (EOS) GmbH of Munich, Germany and has been available commercially since 1995 [1]. Initially the metals and alloys produced by this technology were limited, however more materials options are currently being produced by the DMLS process. These include steel, stainless-steel, tool steel, aluminium, bronze, cobalt-chrome, and titanium-based alloys [2]. Among these materials Ti6Al4V is the most widely applied AM alloy. This is mainly due to its range of applications in the aerospace and the biomedical industries, which is based on by its array of desirable properties, such as good fracture toughness, high specific strength, and biocompatibility [3–5].

Traditionally, turbine-engine fan blades of jet engines have been made from forged Ti6Al4V attached to a forged disk that was usually made of the same material [4]. Small-diameter engines use solid Ti6Al4V blades, whereas larger diameter engines use hollow blades of Ti6Al4V alloy [4]. Conventional processes, such as forging, involve deformation at room temperature or even at high temperatures to obtain better mechanical properties

by breaking up the α -lamellar microstructures and decreasing the size of recrystallized grains. Mechanical working of the AM parts may not be necessary, as the technology aims at producing near net shape components with minimal machining. Other benefits of AM have been identified over forging and other traditional manufacturing processes such as machining and casting. These include reduced material usage, no requirements of hard tooling, manufacturing of parts with complex geometries such as internal cooling passages, and reduced lead time [4–7]. Due to the advantages offered by AM technology, it is being pursued globally by material scientists and engineers as a potential alternative to conventional manufacturing processes. It is worth noting that the current state of research is not essentially about influencing the choice of AM over conventional manufacturing methods, but rather to establish how the AM process may be implemented at different stages in production, where it is deemed advantageous.

Although AM technology offers the noted advantages, the mechanical properties of AM Ti6Al4V are not always as good as those achieved by traditional manufacturing processes. This is mainly because AM results in microstructures that typically differ from those produced by these traditional processes. Additive manufacturing produces a fine microstructure commonly referred to as acicular martensite, which is attributed to rapid solidification because of rapid heat conduction from the localized molten zone towards the surrounding environment. Post-process heat treatment has been routinely applied to these as-built parts to modify the microstructure and consequently optimize their mechanical properties [8–10].

Aircraft components are exposed to complicated loadings during flights. During steady-state conditions, static loads act on structural components. However, dynamic loads are very prominent during the flight phases such as landing [11]. In addition, aircraft structures are expected to respond to extreme conditions of impact such as bird strike and damage from gravel stones during bump taxiing or take-off [12]. While considering the mechanics of an aircraft during landing, the vertical component of its velocity is normally reduced to zero in a very short time and thus this deceleration introduces inertia loads over the structures. Vibration may also be excited by the impact loading through the landing gear, especially in large aircraft with heavy engines installed in the wings. These vibrations also introduce additional inertia loads. The inertia introduced in aircraft creates a critical design consideration for the structures [13]. Foreign object damage (FOD) to fan blades of aircraft engine and the fan-blade out (FBO) events have also been identified as main factors affecting safety in the operation of jet engines [14,15]. Fan blades are susceptible to impact from hard objects like stones and gravel and studies have shown that the damage related to FOD occurs in the form of cracks in damaged zones and dynamic deformation of blades [14,16]. Loss or detachment of blades or parts of the blades when the engine is running includes all the nonlinearities of structural dynamics such as high strain rate plastic deformation of materials and dynamic interaction between turbo-engine structural components [15]. The preceding discussion suggests the need to develop knowledge on the high strain rate deformation properties of additively manufactured Ti6Al4V(ELI). Such a pool of knowledge will provide the aircraft industry with a strong basis of testing the suitability of such AM material for bearing different types of mechanical loads.

The strength and failure of materials are not entirely dependent on the properties of materials, but are rather strongly influenced by stress state, strain rate and temperatures. The strain rate and temperatures strongly influence the dislocation mechanics of a material. High strain rate causes instantaneous strain hardening, thus increasing the yield strength, whereas increasing temperature increases the activities of dislocations and provides sufficient activation energy for the annihilation of dislocations, thus decreasing flow stress [17,18]. Fundamentally, deformation of materials at intermediate strain rates ($>10 \text{ s}^{-1}$) and high strain rates ($>500 \text{ s}^{-1}$) is different from that at quasi-static conditions ($<10 \text{ s}^{-1}$). At quasi-static conditions, static equilibrium is almost invariably maintained as any element in a material in this state has a summation of forces acting on it tending to zero (the inertia force is very small and can be ignored). However, at dynamic and high strain

rates, deformation stresses travel through materials very fast and over small durations, and therefore inertial force is induced. Moreover, dynamic and high strain rates affect thermally activated mechanisms in materials and may result in microstructural changes through adiabatic heating, which make them behave perfectly plastic [19].

More recently, efforts have been made to study the dynamic properties of Ti6Al4V(ELI) produced by various AM technologies. Peng-Hui et al. [20] investigated the thermo-mechanical properties of Ti6Al4V produced by laser deposition-additive manufacturing technology (LDAM) at a wide range of strain rates and temperatures. The effects of porosity on deformation and fracture behaviour under static and dynamic loading of the Ti6Al4V produced by laser-engineered-net shaping (LENS) technology was investigated by Biswas et al. [21]. The effects of building direction on microstructure, dynamic mechanical properties, and deformation mechanisms of electron beam melted Ti6Al4V was presented by Alaghmandfard et al. [22]. Fadida et al. [23] investigated the tensile response of dense and porous AM Ti6Al4V parts under quasi-static and dynamic conditions. Most of these studies have focused on dynamic properties of as-built additive manufactured Ti6Al4V alloy parts. To the best knowledge of the authors, no work has been done on the effects of various heat treatment strategies on the dynamic mechanical behaviour of DMLS Ti6Al4V(ELI). The authors' previous work in References [24,25] focused on the effects of stress relieving heat treatment on high strain rate and impact toughness of direct metal laser sintered (DMLS) Ti6Al4V(ELI).

The aim of this study is to investigate the high strain rate deformation behaviour of various microstructures of DMLS Ti6Al4V(ELI) formed through different heat treatment strategies. The split Hopkinson pressure bar experimental test was used to carry out dynamic testing at strain rates of 750, 1500 and 2450 s⁻¹, and test temperatures of 25, 200 and 500 °C. The microstructure of the undeformed and deformed surfaces, as well as fracture surfaces, were studied using scanning electron microscopy (SEM).

2. Materials and Methods

2.1. Production of Test Specimens

Cylindrical rods with a diameter 6 mm and a height of 80 mm were fabricated from gas atomised spherical Ti6Al4V(ELI) alloy powder, using the EOSINT M280 DMLS machine (EOS GmbH, Munich, Germany). The chemical composition of this powder [26] is shown in Table 1. The optimised set of process parameters shown in Table 2 was used based on research work carried on this equipment to obtain the best mechanical and physical properties of Ti6Al4V(ELI) [27].

Table 1. Chemical composition of Ti6Al4V(ELI) alloy powder as determined in [26].

Element	Al	V	Fe	O	C	N	H	Ti
Composition (wt %)	6.34	3.944	0.25	0.082	0.006	0.006	0.001	Bal.

Table 2. EOSINT M280 DMLS processing parameters.

Processing Variable	Value
Laser power setting	175 W
Laser diameter	80 µm
Hatch spacing	100 µm
Layer thickness	30 µm
Scanning speed	1400 mm/s

The SHPB test specimens were fabricated along the build direction. A photographic image of these specimens on the EOS M280 machine platform is shown in Figure 1. The specimens were first stress relieved at a heat treatment temperature of 650 °C for 3 h followed by furnace cooling, while attached to the base plate. The cylindrical rods were then cut-off from the steel base plate using an electrical discharge machine (wire cutting),

ready for further heat treatment using a SuperSeries™ vacuum furnace system, Model SS12-24/13MX, with a horizontal vacuum chamber. These cylindrical rods were further subdivided into three groups designated as samples C, D and E for further heat treatment. These subsequent heat treatment cycles are summarized in Figure 2. The designations samples A and B were reserved for the reference microstructures of the as-built and stress relieved material, which were presented and discussed in the authors previous work in Reference [28]. The further details on criteria for selection of these heat treatment cycles for DMLS Ti6Al4V(ELI) shown in this figure can also be found in [28].

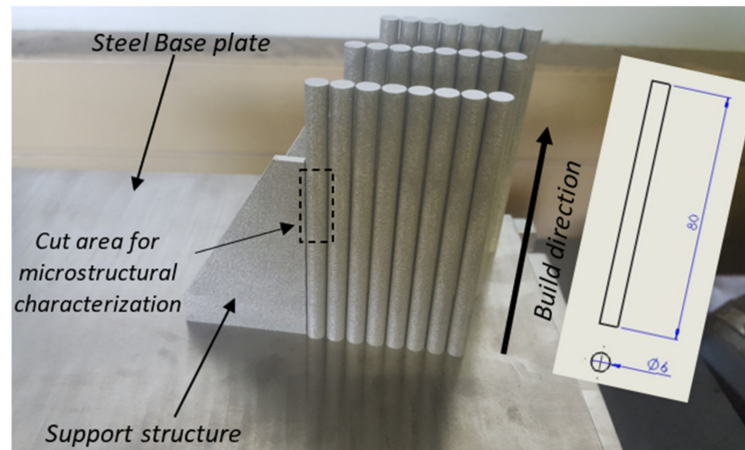


Figure 1. A photographic image showing the manufactured cylindrical rods of Ti6Al4V(ELI) on the EOS M280 machine platform. The insert schematic drawing shows the length of the rods in millimetres.

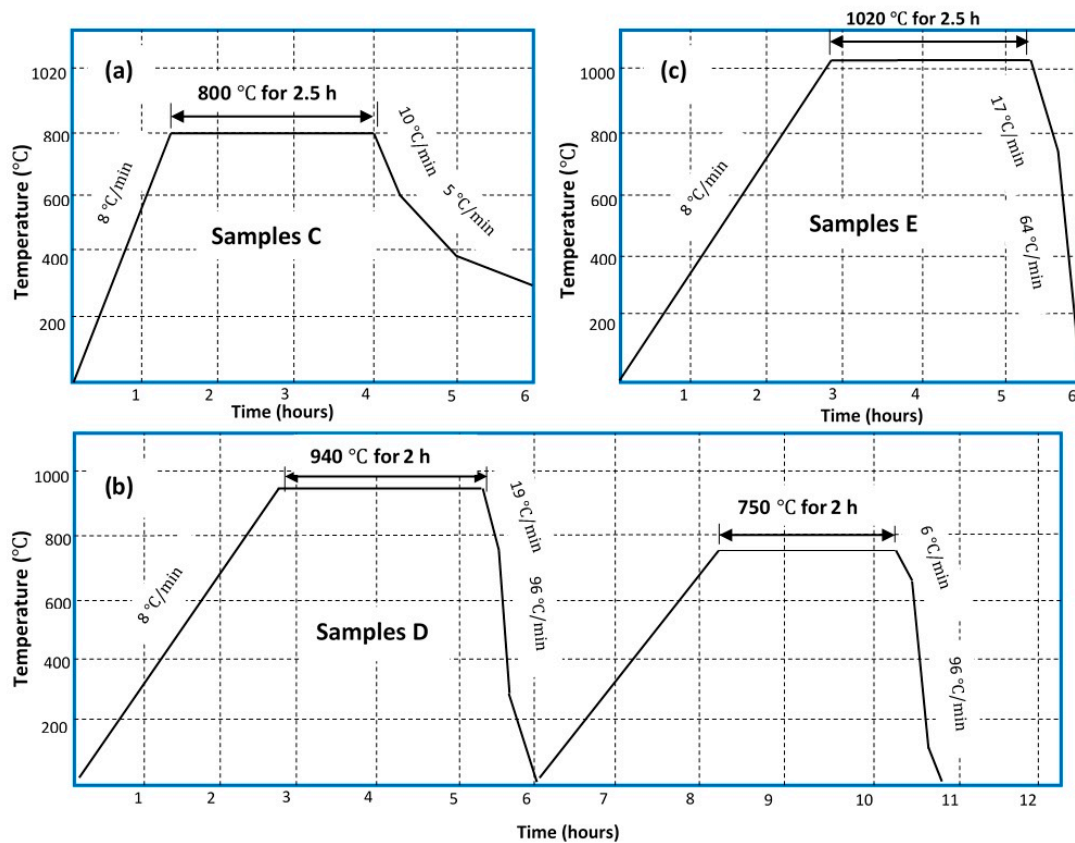


Figure 2. Heat treatment cycles for high temperature annealed DMLS Ti6Al4V(ELI) for (a) samples C, (b) samples D and (c) samples E, all after the initial stress relieving heat treatment.

Specimens for SHPB testing, with a diameter and height of 6 mm were cut from the heat-treated cylindrical rods. These specifications of their dimensions were adopted to ensure an aspect ratio of 1. The 0.5 to 1.5 aspect ratio for SHPB test specimens was shown to represent an optimal balance between reducing the longitudinal inertia effect by using a shorter specimen and reducing radial inertia by using a thinner specimen [29]. The ends of these cut specimens were faced off on a lathe machine to ensure that they were flat and parallel, to ensure the best possible contact between specimen and pressure bars during impact.

2.2. High Strain Rate Experimental Test

The compression split Hopkinson pressure bar (SHPB) test was used in the present research for high strain rate tests. The tests were conducted at the Armaments Corporation of South Africa (ARMSCOR) laboratories in Pretoria. A typical schematic diagram of the SHPB apparatus is shown in Figure 3. The SHPB experimental setup normally consists of a gas gun/cannon, the incident, transmitter, and striker bars as shown in Figure 3. The SHPB test specimen is normally sandwiched between the incident and transmitter bars. During testing, the striker bar is fired from the gas gun/pneumatic launcher and impacts the free end of the incident bar at a high velocity. The impact of the striker bar on the incident bar sends a compressive wave towards the sandwiched specimen. Upon reaching the specimen, the incident wave becomes partially reflected due to impedance mismatch of the bar-sample interface, and partially transmitted to the transmitter bar. The wave reflections occur continuously across the length of the sample until the stress build-up is sufficient to cause plastic strain [30,31].

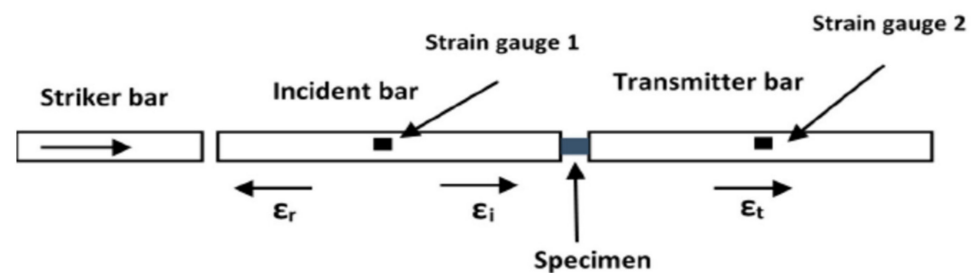


Figure 3. Schematic diagram of the SHPB apparatus in which symbols ϵ_i , ϵ_r and ϵ_t denote the incident, reflected and transmitted waves.

The strain in the incident and transmitter bars is measured by the strain gauges that are attached at the mid points of the surface of each bar so that the incident and reflected waves do not overlap [30]. The equations for determining the samples stress (σ_s), strain (ϵ_s) and strain rate ($\dot{\epsilon}_s$) from the wave signal are based on the theory of one-dimensional elastic wave propagation in a cylindrical specimen, and are as follows [29–31]:

$$\sigma_s = EA_0\epsilon_t / A_s \quad (1)$$

$$\epsilon_s = 2C_0/l_s \int_0^t \epsilon_r dt \quad (2)$$

$$\dot{\epsilon}_s = 2\epsilon_r C_0 / l_s \quad (3)$$

where the symbols A_0 , A_s , l_s , C_0 and E stand for the cross-sectional area of the bars, initial cross section area of the specimen, length of the specimen, bars longitudinal wave velocity and Young's modulus of the bars, respectively. It is important to note that C_0 is the pressure bars' longitudinal wave velocity, a function of the elastic modulus and density (ρ) of the material ($C_0 = \sqrt{E/\rho}$). These are input parameters of the SHPB test.

In the present study, the incident and transmitter bars used for testing of the Ti6Al4V(ELI) alloy specimen were made of tool steel and were 2000 mm long with a diameter 20 mm. The striker bar was made of the same material and same diameter as the pressure bars but

was 500 mm long. The data acquisition system consisted of strain gauges with a gauge factor of 1.88, calibrated voltage of 1.00 V, an amplifier and a data acquisition card fixed in a computer. Hottinger Baldwin Messtechnik GmbH (HBM) strain gauges were arranged in a full Wheatstone bridge configuration to eliminate the effects of bending and only measured the axial strain. The strain gauges were glued at the centre of the incident and transmitter bars (1000 mm from each end) before being wired to the data acquisition card in the computer. A high-speed camera and velocity sensors were used to measure the velocity of the projectile (striker bar) just before it struck the incident bar. To minimize friction and therefore maintain a uniaxial state of compression, lithium based NLGI 3 grease (Castrol WB) was used to lubricate the interface between the pressure bars and the test specimen.

The approach adopted in performing the SHPB high temperature experiments was to heat each test specimen alone in a furnace to the desired temperature, and then bring the bars into contact with the specimen just before impact. The drawback of this approach is the duration of time during which the input bars are in contact with pressure bars before the arrival of the incident wave since prolonged times may reduce the test temperature of the specimen. Therefore, to compensate for any temperature drop by the specimen before impact, the test specimens were soaked at a temperature 30 °C higher than the intended test temperatures.

The specimens were loaded at three different impact velocities of 8, 15 and 25 m/s generated by firing the striker bar at pressures of 4, 7 and 13 bars, respectively. The tests at each strain rate were conducted at three different temperatures of 25, 200 and 500 °C.

2.3. Microstructural Characterisation

Prior to the high strain rate tests, microstructural analysis of the heat-treated samples was carried out. The samples for microstructural analysis were cut from the middle area along the height of the cylindrical rods. Small pieces with a height of 12 mm were cut using EDM wire cutting through the diameter in this area (see Figure 1) of the samples and then sectioned into halves, across the diameter. It should be noted here that the sectioning of these cut specimens was along the build direction. After high strain rate testing the specimens that did not fracture were also mid-sectioned across their diameters for microstructural analysis.

The cut surfaces were mounted using conductive Bakelite and the grinded, followed by chemical-mechanical polishing. The polished surfaces were cleaned individually under tap water, and dried thereafter using a strong stream of compressed air. The surfaces for microstructural analysis in SEM, were then etched in an ESCO Ductless Fume Hood using a solution of Kroll's reagent composed of 2 mL hydrofluoric acid, 6 mL of nitric acid and 92 mL of water. The surfaces for crystallographic texture analysis using a SEM equipped with a backscatter electron detector were not etched, as in this method grain boundaries are delineated by processing of orientation measurement data.

The fracture surfaces of those specimens that failed were first cleaned in an ultrasonic cleaner for about 4 min, using ethanol as the cleaning solvent. These surfaces were then rinsed under running water and then dried using a stream of compressed air. The prepared surfaces of undeformed, deformed and fractured specimens were examined using a JEOL JSM -7001F SEM. The determination of the microhardness of undeformed surfaces was performed using a Future Tech Vickers hardness tester. A 200 g load, with a dwell time of 10 s was used and a minimum of 30 indentations made randomly on the polished surfaces of each specimen.

3. Results

3.1. Microstructural Features of Heat-Treated DMLS Ti6Al4V(ELI) Samples

The secondary electron images (SEIs) and EBSD orientation distribution maps of DMLS Ti6Al4V(ELI) specimens that were exposed to the heat treatment strategies shown in Figure 2, are presented in Figure 4.

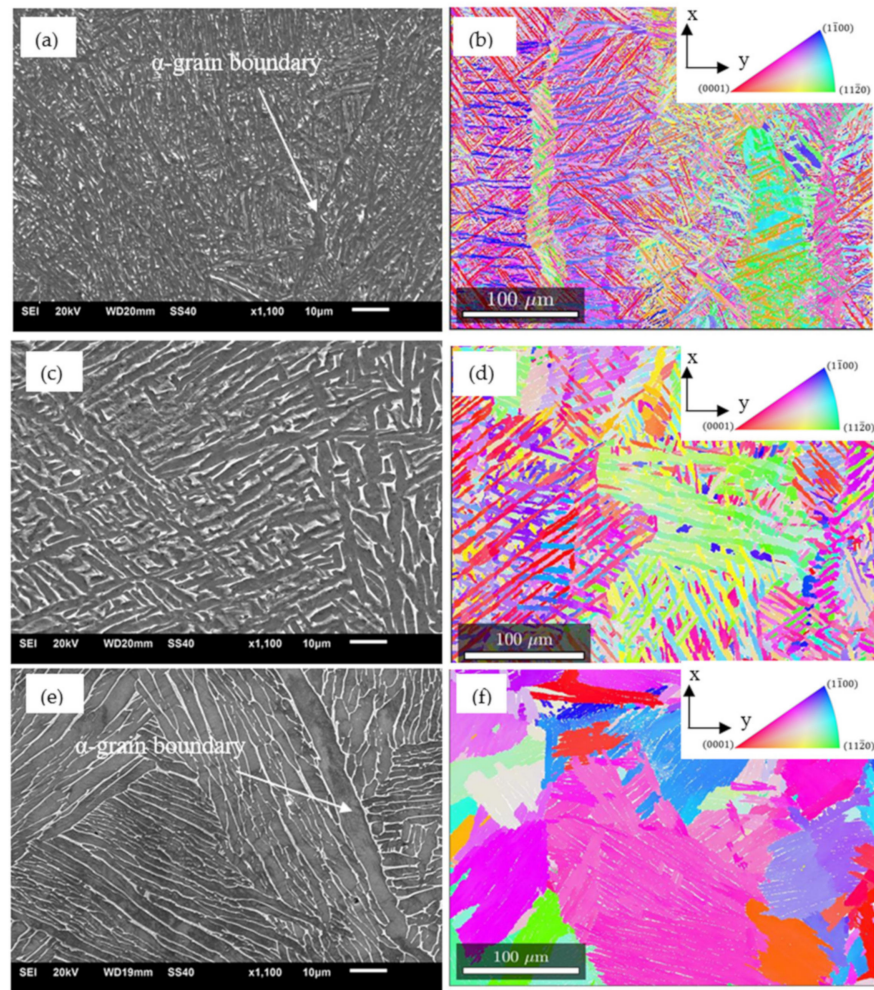


Figure 4. (a,c,e) Secondary electron images and (b,d,f) EBSD orientation maps of (a,b) samples C, (c,d) samples D, and (e,f) samples E, respectively. The inserts in (b,d,f) are keys for the inverse pole figures (IPF).

Samples C were heat treated at 800 °C followed by furnace cooling (FC). During this heat treatment process, the well-known fine acicular α' microstructure associated with as-built DMLS parts [24,25] transformed to an equilibrium mixture of α and β phases as shown in Figure 4a. The average width of α -lathes for samples C measured about 2.5 μm . Samples D, that were exposed to duplex annealing (940 °C/FC followed by 750 °C/FC) had a coarse bi-phasic microstructure as seen in Figure 4c. The average width of the α -lathes in this microstructure was about 6 μm , which was an increase of about 140% in width from the value recorded for samples C. The shape of the α/β grains in samples D was lamellae-like in contrast to the partial particle-like morphology of samples C.

The samples E were heat treated at a temperature above the $\alpha \rightarrow \beta$ transformation temperature and consisted of typical Widmanstätten microstructure with large α colonies as seen in Figure 4e. These colonies contained several parallel α plates where their sizes were limited by the adjacent α colonies. The width of the α lathes within these colonies range between 7–15 μm , with an average width determined through the line-intercept method of 9 μm . A much thicker grain boundary α can be observed at prior β boundaries having a thickness of about 10 μm (Figure 4e).

It is important to note that the β -phase is shown in Figure 4a,c,e as brighter regions that are rich in vanadium, while the regions that are low in vanadium content (α -phase) appear darker. The fraction of β -phase for the bulk microstructure was determined in the

authors previous work [28] through the X-ray diffraction (XRD) method as 3.6%, 6.4% and 6.6% for samples C, D and E, respectively.

The crystallographic orientations of the α -lathes in samples C, D and E are illustrated by the EBSD orientation maps in Figure 4b,d,f. The prior β -grains elongated along the X-build direction are distinct in samples C (Figure 4b) and samples D (Figure 4d), while in samples E (Figure 4e) the columnar grains are seen to have disappeared. The decomposition of the prior β -grains in samples E is a result of heat treatment at a temperature above the $\alpha \rightarrow \beta$ transformation temperature. The IPF shown in the insert of Figure 4b,d,f has a colour code related to specific orientations: the colours red, green and blue represent the family of planes $\{0001\}$, $\{11\bar{2}0\}$ and $\{1\bar{1}00\}$, respectively, parallel to the surface X-Y. Samples C and D exhibit random texture of the α -lathes, however, the crystallographic orientations of some α -lathes tend to repeat within the same prior β -grains as indicated by repetition of the same colour of α -grains. As noted in Figure 4f, the colonies of α -lathes within the equiaxed and semi-equiaxed morphologies in samples E, consist of crystals with a similar orientation, shown by the same colour.

3.2. Micro-Hardness Test Results

The values of micro-hardness of the heat-treated samples of DMLS Ti6Al4V(ELI) and their variation with heat treatment temperature are plotted in Figure 5.

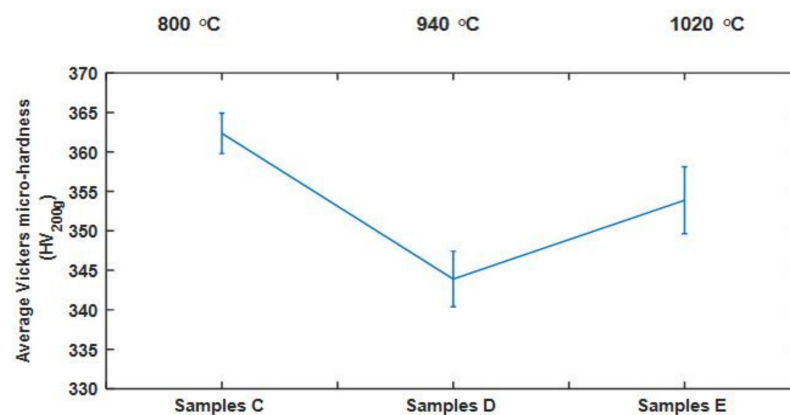


Figure 5. The average Vickers micro-hardness of various forms of DMLS Ti6Al4V(ELI) and their variation with heat treatment temperature.

Samples C recorded the highest value of Vickers micro-hardness, as expected due to the small sizes of α -lathes seen in Figure 4a,b. A decline in hardness is noted upon heat treatment of specimens D at 940 °C and this group of samples recorded the lowest values of micro-hardness. This loss in hardness is attributed to the growth/coarsening of α -lathes seen in Figure 4c,d, because of heat treatment just below the $\alpha \rightarrow \beta$ transformation temperature. Surprisingly, a gain in hardness is then seen to occur in samples E that were heat treated just above the $\alpha \rightarrow \beta$ transformation temperature even though these samples recorded the highest average size α -lathes. It was found in the authors' previous studies [28] that the dislocation density for samples that were heat treated above the $\alpha \rightarrow \beta$ transformation temperature was higher than in samples D, but lower than the values in samples C. The authors attributed the increase in dislocation density to the increase in percentage of low angle grain boundaries (LAGBs) which are dislocations in nature. This could lead to the increase of hardness seen in Figure 5, as the LAGBs offer increased resistance to localized plastic deformation induced by mechanical indentation.

3.3. High Strain Rate Behaviour of Various Forms of DMLS Ti6Al4V(ELI) Alloy

3.3.1. Stress-Strain Characteristics

High strain rate tests were conducted for a range of temperatures from ambient condition (25 °C) to 500 °C. The strain rates were controlled by regulating the pressures

used to launch the SHPB projectile/striker bar. Different pressures affected the velocity of the striker bar, differently, which led to the generation of different strain rates. Pressures of 4 bars, 7 bars and 13 bars generated striker velocities recorded by velocity sensors and a high-speed camera of 8, 15 and 25 m/s, respectively. Figure 6 shows that these velocities deformed the material at average true strain rates of about 750, 1500 and 2450 s⁻¹, in order of increasing velocity. Figures 7–9 present the dynamic true stress–strain and true stress–temperature curves of samples C, D and E, each of which were deformed at average true strain rates of 750, 1500 and 2450 s⁻¹, and at temperatures of 25, 200 and 500 °C.

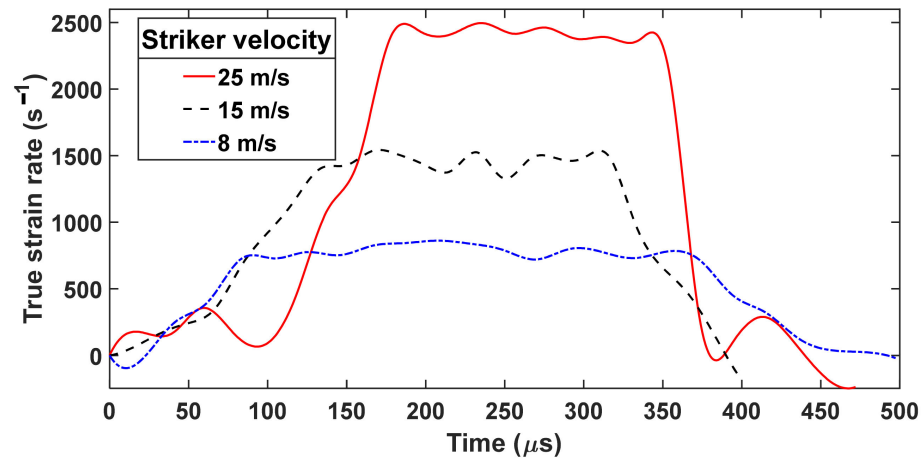


Figure 6. Strain rate-time graphs generated at different SHPB striker bar velocities.

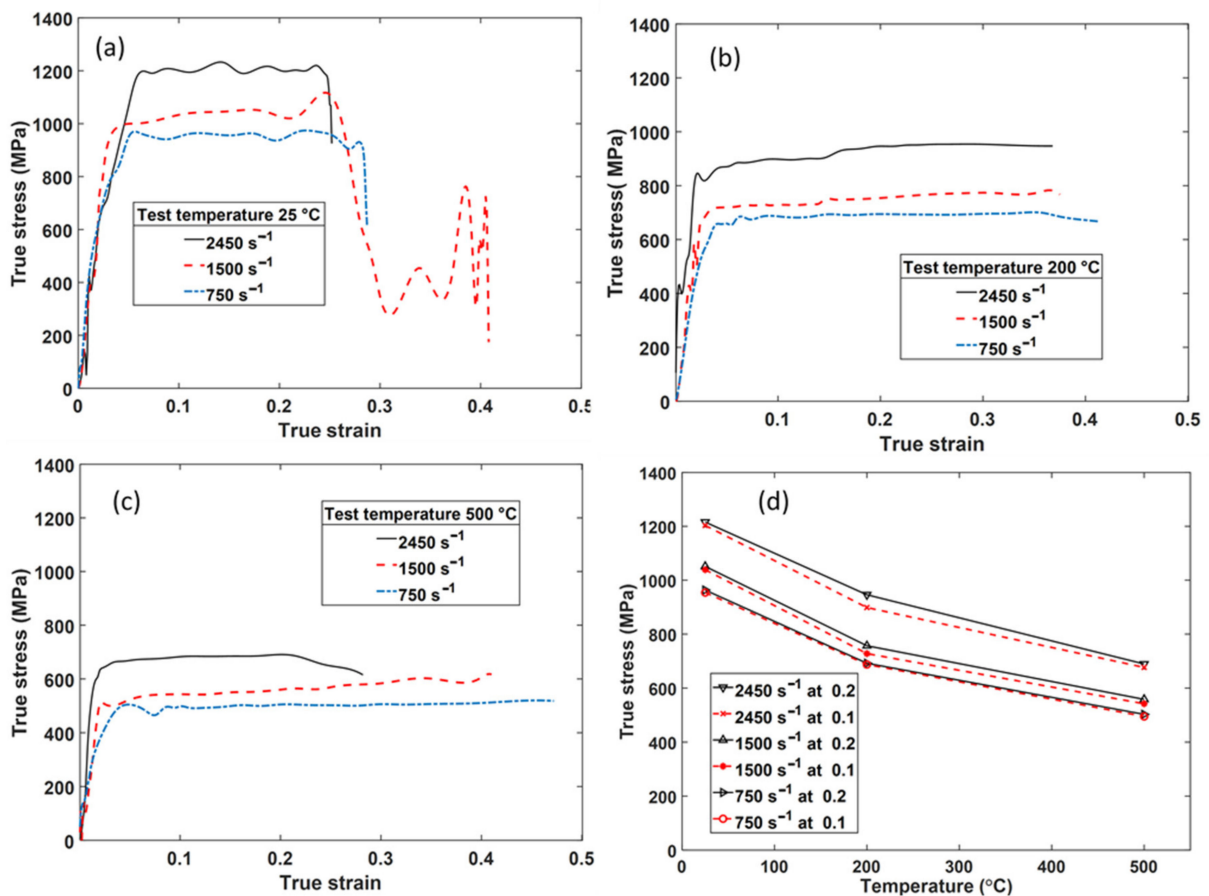


Figure 7. The true stress–strain curves (a–c) at different strain rates and temperatures, and (d) true stress vs. temperature curves at different strain rates and at strains of 0.1 and 0.2, all for samples C.

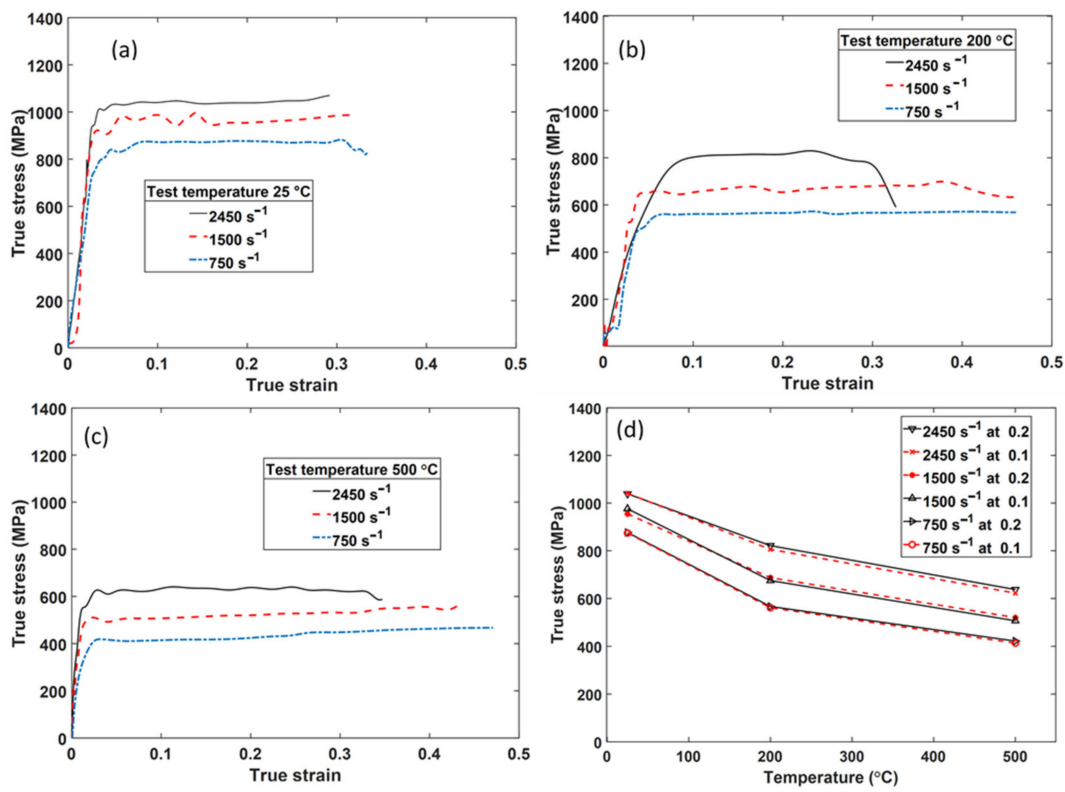


Figure 8. The true stress–strain curves (a–c) at different strain rates and temperatures, and (d) true stress vs. temperature curves at different strain rates and at strains of 0.1 and 0.2, all for samples D.

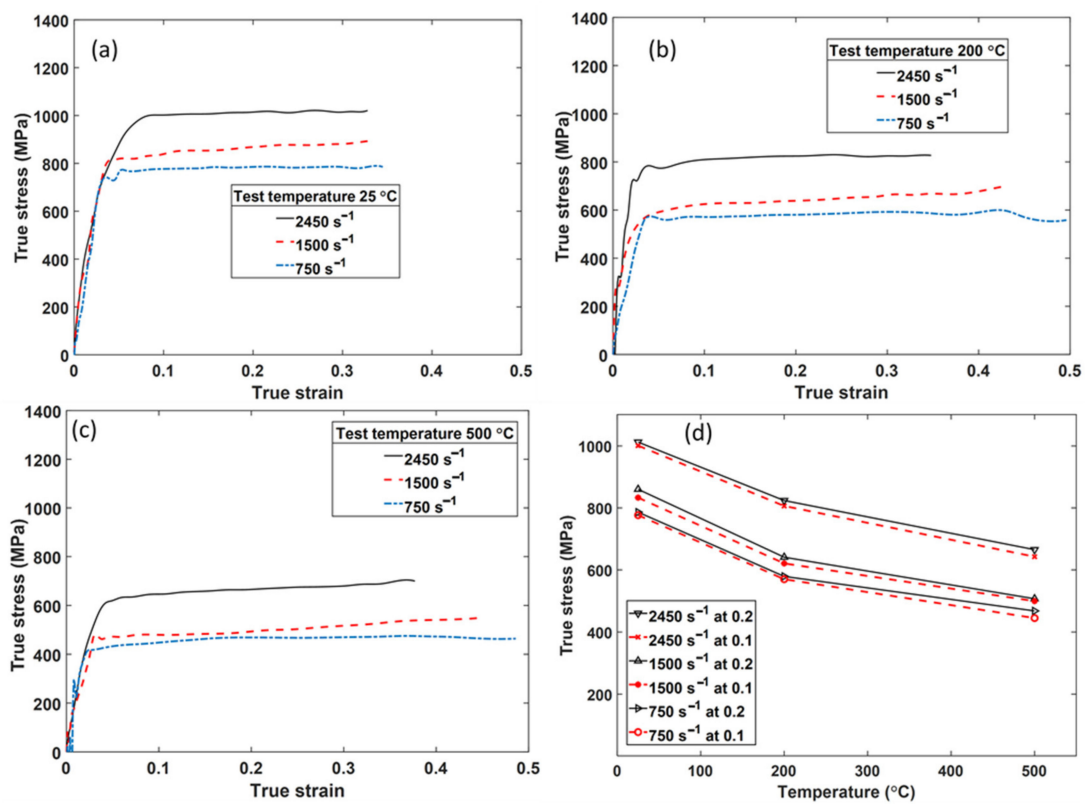


Figure 9. The true stress–strain curves (a–c) at different strain rates and temperatures, and (d) true stress vs. temperature curves at different strain rates and at strains of 0.1 and 0.2, all for samples E.

A general observation in all curves in Figure 7a–c, Figures 8a–c and 9a–c is that the flow stress increases with increasing strain rate, whereas as shown in Figures 7d, 8d and 9d, it decreases with increase in temperature. Figures 7d, 8d and 9d also show that the flow stresses are generally lower at lower values of strain. These observations clearly show that these three different microstructures of DMLS Ti6Al4V(ELI) are sensitive to strain, strain rate and temperature. The observed increase in flow stress with increase in strain rate can be attributed to increased generation and interaction of dislocations causing higher instantaneous strain hardening at and beyond yield, thereby increasing flow stress in the material. Whereas, for tests conducted at elevated temperatures, the generation of dislocations is countered by the annihilation of dislocations, a phenomenon referred to as thermal softening, which then leads to a decline in flow stress. It is also apparent in Figures 7–9 that under these high strain rate loading conditions the three different forms of DMLS Ti6Al4V(ELI) alloys yielded at different levels of stress for the same imposed strain rates and temperatures. This is expected due to the different microstructures of the three groups of samples. Further information on the curves shown in Figures 7–9 and observations made during testing are presented in Table 3.

Table 3. Strain rates, yield stress, state of fracture and fracture strain for the high strain rate flow stress curves of samples C, D and E.

Temperature (°C)	Alloy	Strain Rate (s ⁻¹)	Dynamic Yield Stress (MPa)	Fracture State	Fracture Strain
25	C	750	964	No fracture	-
		1500	1003	No fracture	-
		2450	1204	Fractured	0.25
	D	750	833	No fracture	-
		1500	923	No fracture	-
		2450	1014	Fractured	0.29
	E	750	739	No fracture	-
		1500	810	No fracture	-
		2450	958	Fractured	0.32
200	C	750	607	No fracture	-
		1500	690	No fracture	-
		2450	825	Fractured	0.36
	D	750	529	No fracture	-
		1500	639	No fracture	-
		2450	802	Fracture	0.32
	E	750	581	No fracture	-
		1500	615	No fracture	-
		2450	752	Fractured	0.34
500	C	750	498	No fracture	-
		1500	507	No fracture	-
		2450	641	Fractured	0.28
	D	750	414	No fracture	-
		1500	506	No fracture	-
		2450	616	Fractured	0.34
	E	750	457	No fracture	-
		1500	480	No fracture	-
		2450	626	Fractured	0.37

For ease of comparison of the mechanical properties of the three forms of DMLS Ti6Al4V(ELI), the results in Table 3 are presented in Figure 10. In these high strain rate tests, not all the conditions of strain rate and temperature resulted in specimen failure, as is evident in Table 3. Only the specimens loaded at a strain rate of 2450 s⁻¹ led to fracture. The specimens tested at strain rates of 750 and 1500 s⁻¹, could not reach fracture

strain because the waves generated by these strain rates were not sufficient to load these specimens to failure. It is evident from Equation (2) that the strain experienced by the SHPB test specimen is dependent on the magnitude of the reflected signal amongst the other factors in the equation. As noted earlier, if the duration of buildup of the reflected wave is limited due to low striker velocity the specimen cannot reach the fracture strain.

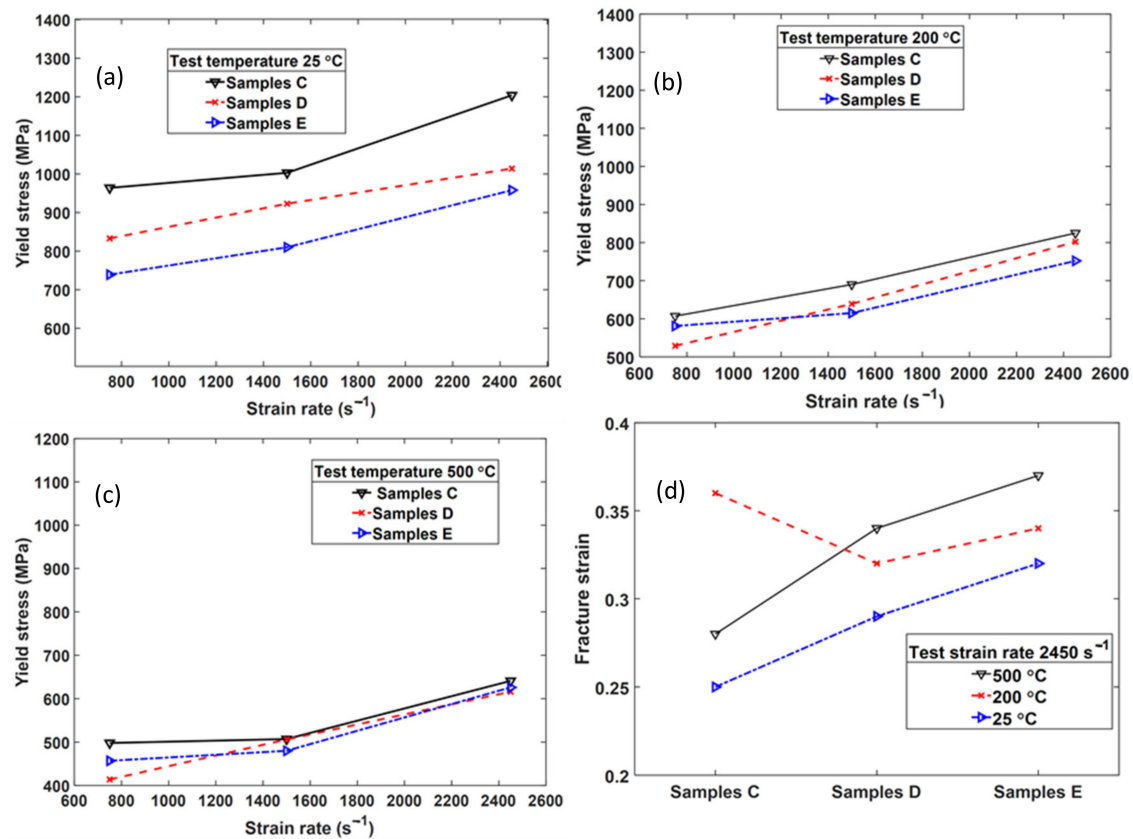


Figure 10. Comparison of (a–c) yield stresses under different high strain rates and (d) fracture strains at the strain rate of 2540 s⁻¹ and different temperatures for samples C, D and E.

As seen in Figure 10a–c, samples C showed the highest yield stress at any given temperature and strain rate as compared to samples D and E. Samples E showed the lowest yield stress compared to the other two groups of samples for most of the test strain rates and temperatures. As further seen in Figure 10d, the fracture strains that were recorded for samples loaded at the highest strain rate of 2450 s⁻¹, were lowest at 25 °C for all samples. The fracture strains of samples E at the highest strain rate were the highest at 25 °C and 500 °C and second highest at 200 °C. The high yield stress in samples C in comparison to samples D and E is attributed to the small average α -lath thickness, recorded as 2.5 μm for samples C, which therefore leads to a short effective slip length during deformation, thus increasing the yield stress and subsequent flow stress.

In previous work by the authors [24], the reference microstructures of DMLS Ti6Al4V(ELI) (as built samples (A) and stress relieved samples (B)) were reported to show much higher strength and low fracture strain compared to the heat-treated samples C, D and E at high strain rates. For instance, these reference samples fractured at a strain rate of 700 s⁻¹ which is slightly lower than the lowest strain rate used in the present study, which as seen in Table 3 did not load the heat-treated samples to fracture. The fracture strain of samples A and B at a strain rate of 700 s⁻¹ was reported as 0.124 and 0.135, respectively [24]. These values are much lower than those recorded for samples C, D and E at the much higher strain rate seen in Table 3. The yield stress of samples A and B at a strain rate of 700 s⁻¹ was reported in this previous work as 1384 MPa and 1402 MPa, respectively [24]. These

values of yield stress are much higher than those of the heat-treated samples C, D and E shown in Table 3, for much higher strain rates. This is anticipated due to decomposition of the α' -martensitic microstructure in samples A and B into an equilibrium mixture of $\alpha + \beta$ phases upon heat treatment above the martensitic transformation temperature.

3.3.2. Strain Rate Sensitivity

To get clarity on the effects of strain rate and temperature on the dynamic response of the various microstructures of DMLS Ti6Al4V(ELI), the variation of true stress with strain rate as a function of temperature was plotted. The effects of strain rate on flow stress at a fixed strain and temperature can be quantified using the strain rate sensitivity parameter m expressed as:

$$m = \frac{\partial \log \sigma}{\partial \log \dot{\epsilon}} \quad (4)$$

where, the symbols σ and $\dot{\epsilon}$ stand for true stress and true strain rate, respectively. The strain rate sensitivity is therefore, given by the slope of the linear plot of true stress vs. true strain rate in \log - \log graphs and at a given strain. Such plots for the samples tested in the present study are shown in Figure 11 for a true strain of 0.1.

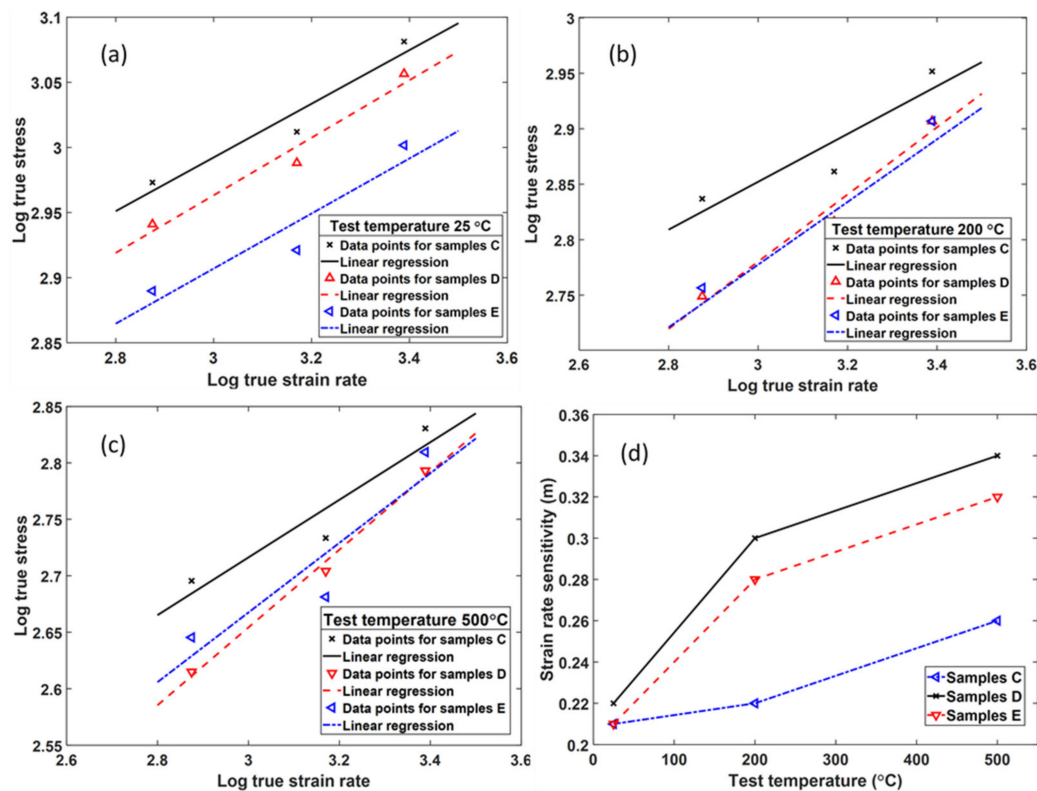


Figure 11. Plots (a–c) true stress vs. true strain rate on a \log - \log scale at a true strain of 0.1, at different test temperatures and (d) the variation of the strain rate sensitivity parameter m with temperature for samples C, D and E.

The increase of flow stress with strain rate of the curves presented in Figure 11, shows a linear dependence as evidenced by the correlation coefficients of the plots presented in Table 4. The strain rate sensitivity parameter m for the three categories of samples at the three test temperatures used for testing here is also shown in the table and for ease of comparison presented in (d) of Figure 11. As seen in Table 4 and Figure 11d the calculated values of strain rate sensitivity m increase with test temperature for all samples tested. Generally, plastic deformation in alloys is mainly due to slip of dislocations.

Table 4. Correlation coefficient (R^2) of the log-log plots of true stress and strain rate, and strain rate sensitivity (m) for samples C, D and E at various test temperatures.

Test Temperature	25 °C		200 °C		500 °C		
	Alloy	m	R^2	m	R^2	m	R^2
C		0.21	0.94	0.22	0.85	0.26	0.89
D		0.22	0.96	0.30	0.97	0.34	0.85
E		0.21	0.89	0.28	0.97	0.32	0.99

Furthermore, the flow stress of materials consists of a thermal part (that is dependent on strain rate and temperature) and an athermal part (generally regarded as being independent of strain rate and temperature) [32]. The thermal part is controlled by short-range barriers, such as mobile dislocations and the Peierls stress and is sensitive to both temperature and strain rate [32–35]. High strain rates accelerate the multiplication of these mobile dislocations, leading to the formation of dislocation tangles [33]. On the other hand, high temperatures will supply the dislocations with sufficient thermal energy to help overcome dislocation tangles, thus enhancing the activities of dislocations [33,34]. Moreover, at high temperatures, edge dislocations of the α -phase in Ti6Al4V(ELI), can climb along the direction perpendicular to their slip planes [35]. Thus, the increase in the magnitude of the strain rate sensitivity parameter m with temperature seen in Table 3 is a sign of an attendant increase in dislocation-activity. The higher value of the strain rate sensitivity parameter at higher deformation temperatures, can also be explained by the increasing activity of the non-basal slip systems as a function of increasing temperature (200 °C to 500 °C in this case), in addition to existing slip in the basal slip systems of the hcp structure of this material.

The athermal part of the flow stress is controlled by long-range barriers such as grain boundaries and the secondary precipitates, which are generally regarded as being independent of the temperature and strain rate during high strain rate deformation [33,34]. This implies that the effects of grain size on the activity of dislocations of this material cannot be ignored. A previous study by Conrands [36] showed that the effect of grain size on strain rate sensitivity is mainly attributed to the thermally activated dislocation motion, since reducing the grain size leads to a decrease in the spacing of dislocation forests, thereby enhancing the parameter m . In fact, for α -lathes with small thicknesses, it means that dislocations inside them move a shorter distance before encountering obstacles (grain boundaries), thus increasing the material's potential of encountering serious dislocation pile ups and hence a higher value of the parameter m . It is important to note here that a high strain rate sensitivity index could mean that the material exhibits a dramatic increase in strength with increase in strain rate, which is consistent with the results presented in Figures 7–9.

The calculated values of the strain rate sensitivity index m shown in Table 4 and Figure 11d do not follow the analogy of grain size described in the preceding paragraph, namely that the strain rate sensitivity increases with decrease in grain size. At any given temperature, samples D (average lathes thickness 6 μm) have the highest strain rate parameter, showing the material to be more sensitive to high strain rate and temperature than the other two types of samples. On the other hand, samples C (average lathes thickness of 2.5 μm) show the lowest response to high strain rate and temperature depicted by a lower value of m . Samples E with the largest average α -thickness have higher values of m at all temperatures and strain rates than samples C, but lower than those of samples D.

A previous study by Mao et al. [37] attributed opposite/reverse grain size dependence on strain rate sensitivity of copper at high strain rate because of a change in deformation mechanisms from obstacle-controlled plasticity to a combination of obstacle and dislocation drag controlled plasticity. A similar case was reported elsewhere in Lesuer [38] for close packed structures. At high strain rates the interactions of mobile dislocations with phonons and electrons slow down the motion of dislocations and therefore more force is

required to deform the material. Generally, a shock wave acting on a material crystal lattice generates mechanical waves within the crystal structure. The unit of vibrational energy that arises from oscillating atoms within the crystal is referred to as a phonon. The Orowan relation [39] can be used to derive pure drag plasticity for a material, from the relationship of the strain rate ($\dot{\epsilon}$), mobile dislocation density (ρ_m) and velocity of dislocations (v) as:

$$\dot{\epsilon} = \frac{vb\rho_m}{M} \quad (5)$$

where M is the Taylor factor. The average dislocation velocity as described in Frost and Ashby [40] can be expressed as:

$$v = \frac{\sigma_{drag}b}{M\mu_d} \quad (6)$$

where σ_{drag} , b and μ_d are the viscous drag flow stress due to the dislocation drag effect, Burgers vector and drag coefficient, respectively. Dislocation density can be assumed to be proportional to the reciprocal of the grain size (d) (taking this as represented by the lath thickness in the case of DMLS Ti6Al4V(ELI)). Furthermore, the mobile dislocation density is part of the total dislocation density, and the scale factor or this proportionality can be assumed constant for the three material variants C, D and E. With these assumptions, Equations (5) and (6) can be combined to give:

$$\sigma_{drag} = \frac{\dot{\epsilon}\mu_d M^2 d}{b^2} \quad (7)$$

For polycrystals, the Taylor factor, M varies from grain to grain due to their differences in texture with reference to the loading axis. Where all the grains undergo the same deformation and based on the use of the von Mises compatibility conditions, Taylor [41] obtained the average value for M as 3 for hcp crystal structures.

The parameter M was therefore taken as equal to 3 in this study for Ti6Al4V(ELI) alloy. Furthermore, the drag coefficient is a constant of proportionality between the applied stress/force and dislocation velocity thus the ratio μ_d/b^2 can be taken as a constant K . Thus, the graphs of flow stress due to dislocation drag effect against strain rate for different grain sizes and against grain sizes for different strain rates are as presented in Figure 12. As seen in this figure the relationship between flow stress and the grain size/lath thickness is one where thicker α -lathes give a higher drag stress and vice versa. This could explain the higher values of index m for samples D and E than those of samples C. While comparing the strain rate sensitivity index of samples D and E it is important to highlight the microstructural and textural differences between these samples as discussed in Section 3.1. Samples D are characterized by typical basket-weave microstructure with α -grains having random orientation. On the other hand, samples E have largely typical Widmanstätten microstructure composed of colonies of α -lathes with similar orientation.

The ease of penetration of dislocations across the α/β interfaces depends upon the degree of alignment of slip directions in adjacent phases as determined by the Burgers orientation relationship (BOR) [42]. As seen in Section 3.1, samples D with the typical basket-weave microstructure have a high number of different α variants in the microstructure making it difficult to transfer slip across the grains. However, for samples E, which are composed of colonies of parallel α -lathes sharing the same crystallographic orientation, it is easier to transfer slip across the lathes and therefore less force is required to initiate plastic deformation. The foregoing discussion suggests that the morphology, texture and atomic-level intrinsic dislocation mechanisms can play an important role in determining the flow response and strain rate sensitivity of the DMLS Ti6Al4V(ELI) alloy.

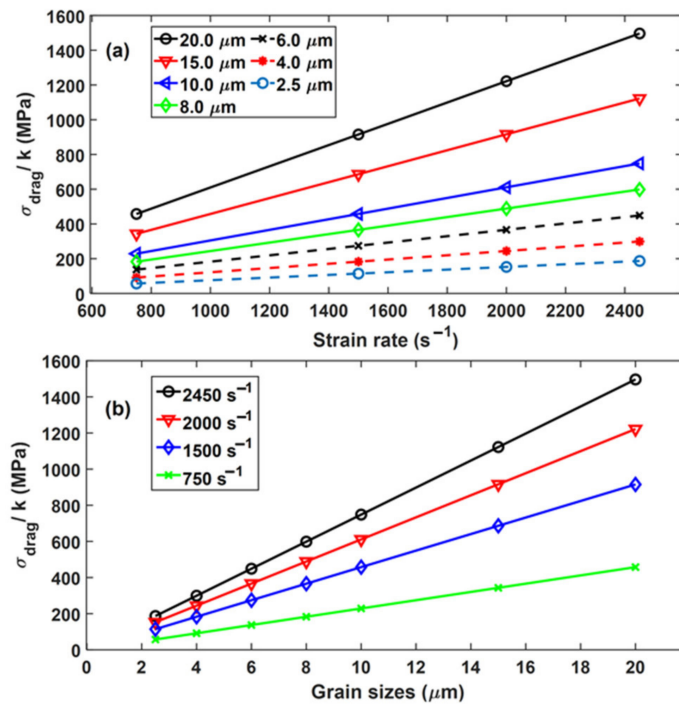


Figure 12. Viscous drag stress as a function of (a) strain rate for different grain sizes and (b) grain size at different strain rates.

3.4. Analysis of Deformed Microstructure and Fracture Surfaces

3.4.1. Analysis of Deformed Surfaces

As previously indicated in Table 2, not all the dynamic test conditions resulted in failure of specimens and only the samples that were tested at a strain rate of $2450 s^{-1}$ failed. As the specimens that were tested at strain rates of 750 and $1500 s^{-1}$ at all test temperatures did not fail, they form a good basis for analysing the deformation characteristics of the various forms of DMLS Ti6Al4V(ELI) alloy. Figure 13 shows the quintessential deformation features of these samples, observed under low magnification in an optical microscope.

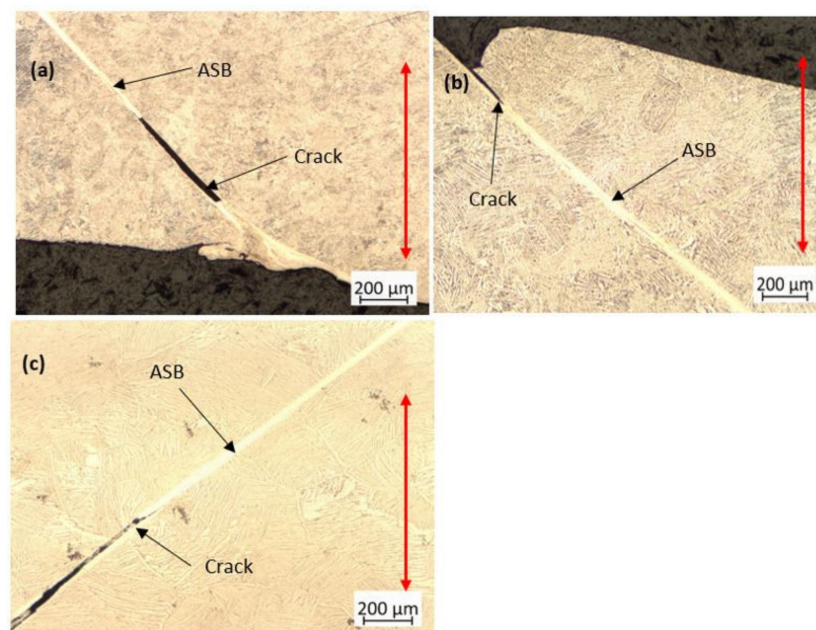


Figure 13. Typical deformation features on cross sections through the surfaces of samples (a) C, (b) D, and (c) E observed under an optical microscope (the red arrows indicate the compression axis).

It is apparent from the micrographs in Figure 13 that the deformed surfaces of various samples of DMLS Ti6Al4V(ELI) are characterised by bright bands and in some places the bright bands are replaced by dark elongated features. The bright bands are known as adiabatic shear bands (ASBs), while the dark elongated features are cracks propagating along the ASBs. The ASBs are seen in Figure 13 to be narrow and to extend through the grains across the deformed surfaces at an angle of approximately 45° to the compression axis, which is the expected angle of maximum shear in cases of uniaxial loading.

Generally, plastic work during high strain rate deformation of materials is invariably transformed into thermal energy, which leads to a rise in the local temperature in a material. Because the thermal conduction of Ti6Al4V(ELI) is very poor, while its strain hardening as seen in Figures 7–9 is low (the plastic deformation curves with relatively low gradients), the alloy is sensitive to strain localization in the conditions of dynamic deformation [43]. The thermal softening effect due to adiabatic or quasi-adiabatic deformation processes at high strain rate lowers the strength of materials during plastic deformation. As the strain increases, the thermal softening effect outweighs the strengthening effect due to strain hardening and shear instability occurs. Basically, if the stress in the primary shear zone is surpassed by the stress in the bulk material, a shear localization event takes place forming narrow shear bands [44]. Once formed, the ASBs become sites of subsequent failure by rapid nucleation and growth of cracks within them as seen in Figure 13. The ASBs in the three forms of DMLS Ti6Al4V(ELI) at different strain rates and temperatures were studied further at higher magnification in a SEM, to give the SEIs presented in Figures 14–16.

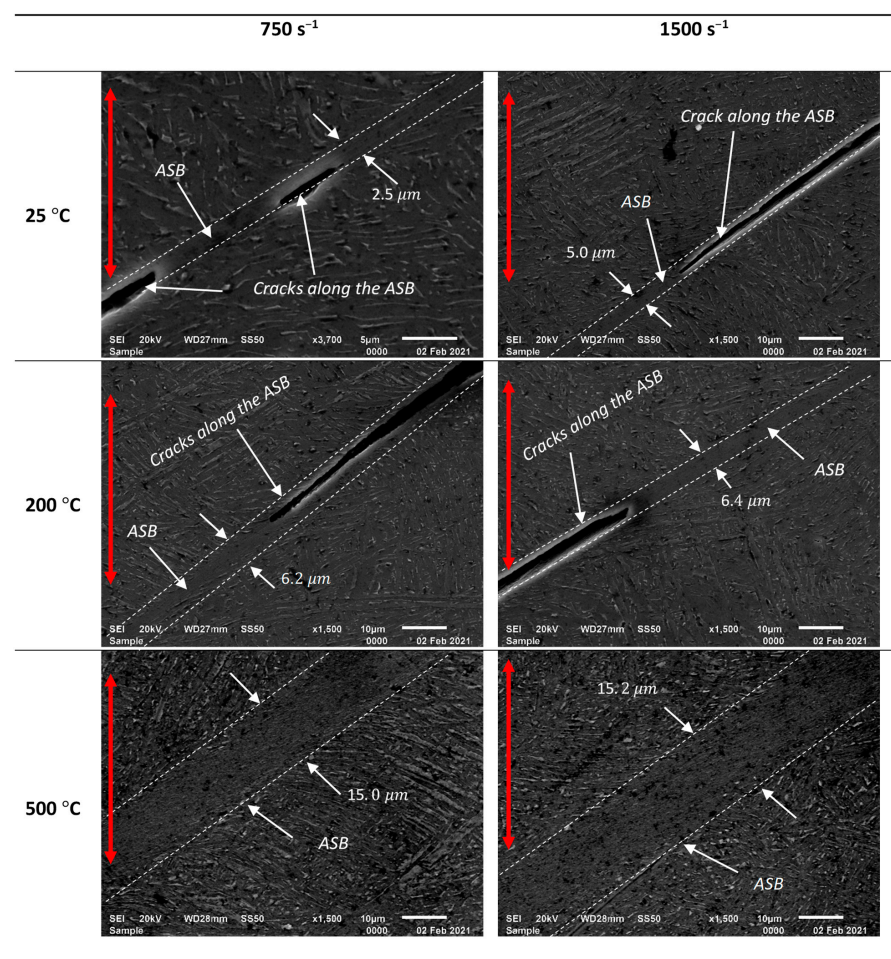


Figure 14. Secondary electron images showing adiabatic shear bands on sections of deformed surfaces of samples C at different strain rates and temperatures (note the different magnification at 750 s^{-1} and $25 \text{ }^\circ\text{C}$). The red arrows indicate the compression loading axis.

It is clear from observation of Figures 14–16 that the microstructures within the adiabatic shear bands are different from that of the bulk material, a difference thought to have arisen during the formation of these adiabatic shear bands. It is known from literature [44,45] that microstructural changes such as dynamic recovery, recrystallization and phase transformation do occur during formation of ASBs. However, a direct evidence of these microstructural changes could not be pinpointed from the SEIs presented in the three figures. The most appropriate method to study the microstructural changes along the ASBs is the EBSD technique. As previously mentioned, the formation of ASBs precedes failure mechanisms such as nucleation and propagation of cracks. As seen in these figures, well-developed ASBs in some cases are accompanied by cracks which propagate within and along the bands. This suggests that the eventual failure of the different forms of DMLS Ti6Al4V(ELI) at high strain rate is because of the formation of ASBs which offer favourable regions for the initiation, growth and propagation of cracks.

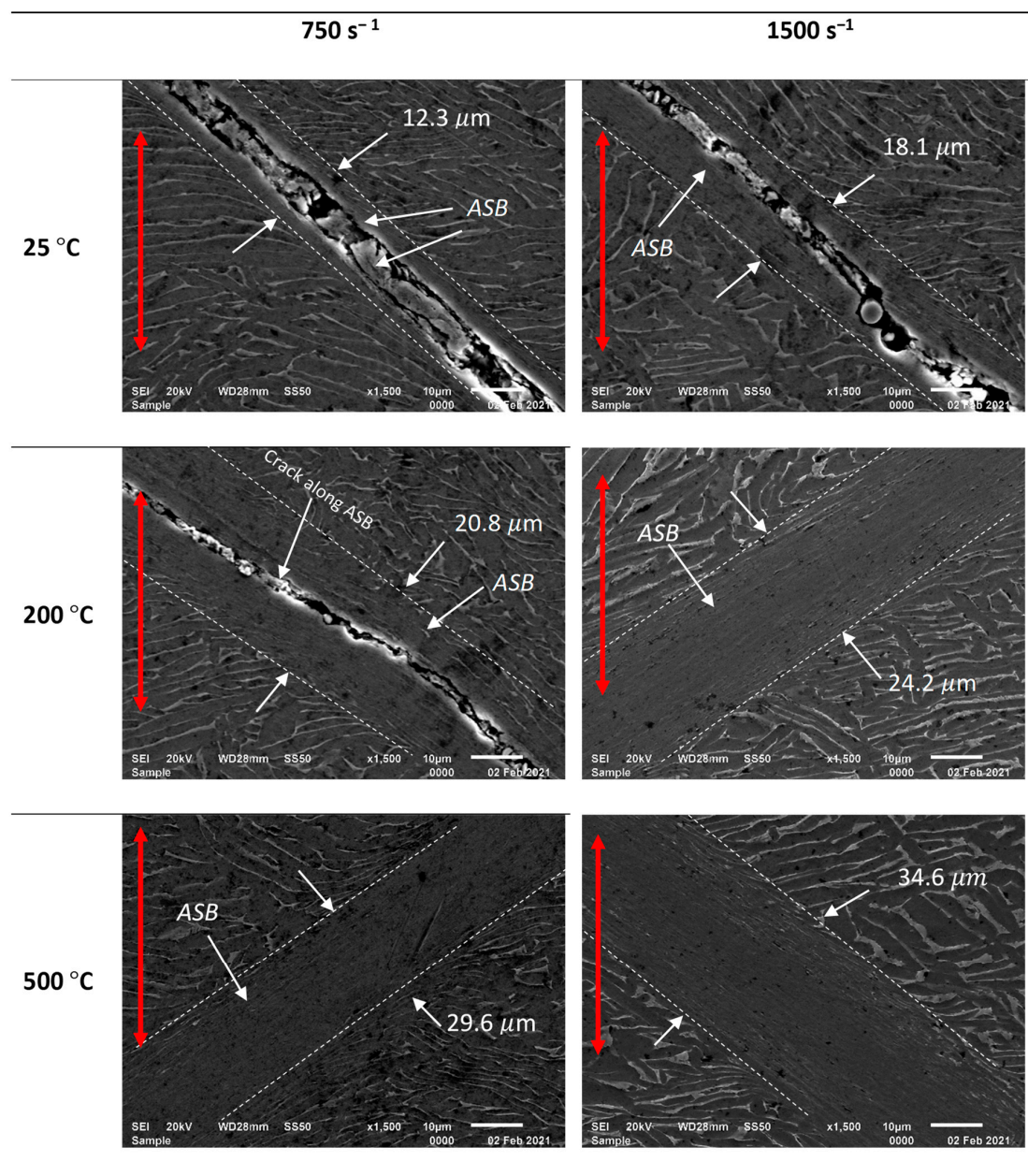


Figure 15. Secondary electron images showing adiabatic shear bands on sections of deformed surfaces of samples D at different strain rates and temperatures (the red arrows indicate the compression loading axis).

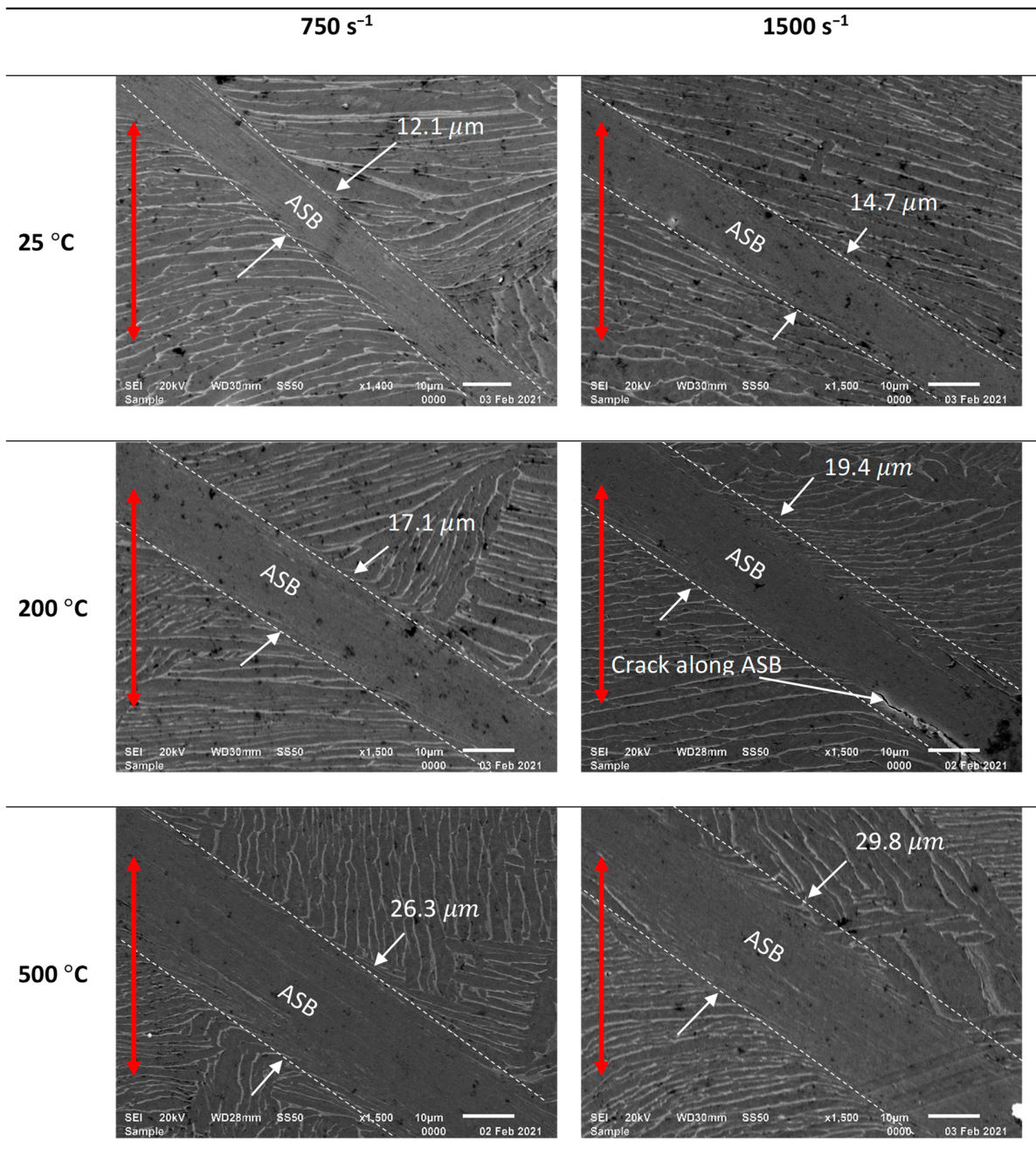


Figure 16. Secondary electron images showing adiabatic shear bands on sections of deformed surfaces of samples E at different strain rates and temperatures (the red arrows indicate the compression loading axis).

The width of ASBs is seen in Figures 14–16 to vary for different forms of the DMLS Ti6Al4V(ELI) alloy and at different test conditions of strain rate and temperature. A summary of the average width of ASBs for different forms of the alloy and at different testing conditions, is presented graphically in Figure 17, all together for ease of comparison.

It is evident from this figure that the average width of the ASBs increases with increasing test temperature, almost invariably in linear relationships. A similar observation was reported by Lee and Lin [46] for wrought Ti6Al4V. The average width of the ASBs is also seen in the figure to increase with strain rate, however, the error bars are seen to overlap which could suggest that the increase in the width of the adiabatic shear bands is not significant between the strain rates of 750 and 1500 s⁻¹.

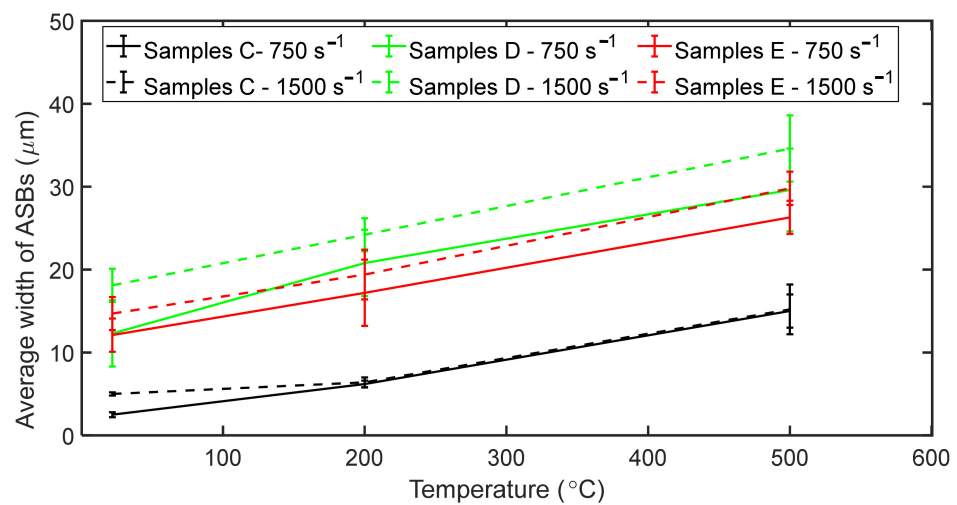


Figure 17. Variation of the average width of adiabatic shear bands as a function of temperature and strain rate for samples C, D and E.

A significant difference in the average width of ASBs is noted in Figure 17 for different samples of DMLS Ti6Al4V(ELI). At the same strain rate and temperature, samples C and D show the lowest and the highest values of width, respectively. This suggests that the heat treatment regimens of DMLS Ti6Al4V(ELI) do influence the width of ASBs formed at conditions of high strain rate deformation. A critical factor that influences the width of ASBs as reported in the research of Dodd and Bai [42] is the hardness of materials, as the width of the ASBs diminishes with increasing hardness of the material. Hardness is generally a measure of a material's resistance to localized plastic deformation and is normally proportional to material strength. The thermo-softening effect which results in the formation of ASBs is expected to reduce with increase in strength and related hardness of materials.

The values of Vickers hardness for samples C, D and E shown in Figure 5 were 362.36 ± 2.57 HV, 343.92 ± 3.52 HV and 353.88 ± 4.23 HV, respectively. This order of hardness is consistent with the order of width of ASBs observed here for the three microstructures. Therefore, the difference in the width of the ASBs observed in Figure 17 for samples C, D and E is because of the different microstructures formed by the different heat treatment processes and the arising values of strength and hardness.

3.4.2. Fractographic Analysis of Failure Surfaces

Figure 18 presents photographic images of the specimens tested at a strain rate of 2450 s^{-1} and at different test temperatures. It is clear from this figure that the specimens failed in a catastrophic manner along a plane oriented at an angle of approximately 45° to the compression axis. From the observation made in the preceding section, it is plausible to deduce that the specimens fractured because of intensive localized shear flow prompted by the formation of adiabatic shear bands, seen in Figures 14–16, which were also inclined at an angle of approximately 45° .

The effects of temperature are also revealed in Figure 18 where at 200°C and 500°C the specimens were seen to have undergone more plastic deformation in comparison to those deformed at a temperature of 25°C . Figure 19 shows the measured height of deformed specimens and corresponding longitudinal plastic strain at a strain rate of 2450 s^{-1} and at different temperatures. From Figure 19, the measured deformed height and corresponding longitudinal plastic strain for different specimens are seen to decrease and increase with temperature, respectively.

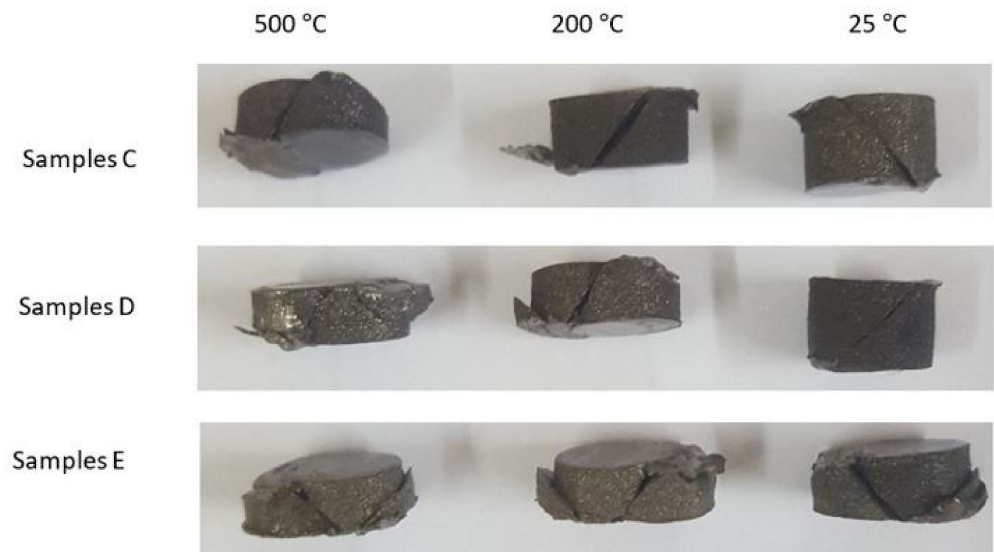


Figure 18. The photographic images of specimens deformed at a strain rate of 2450 s^{-1} and at temperatures of 25, 200 and 500 °C.

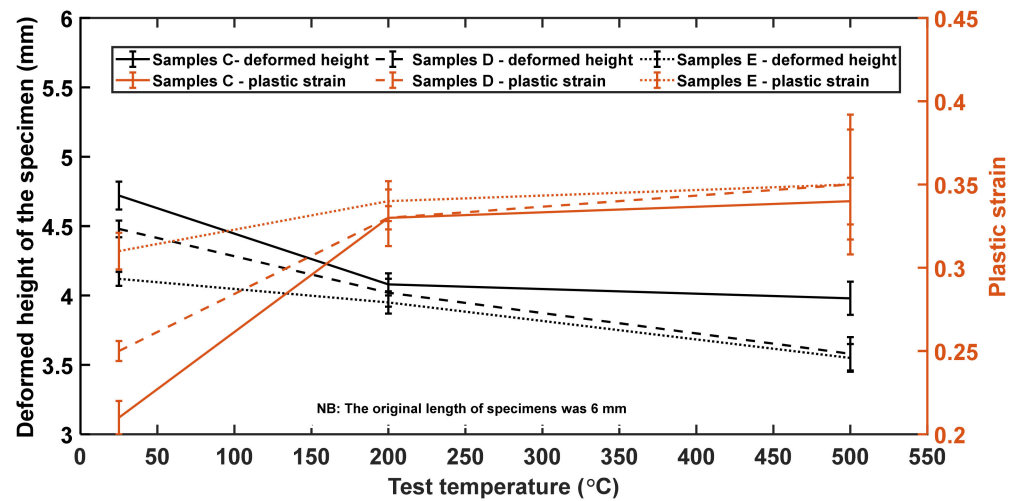


Figure 19. The measured height of deformed specimens and estimated longitudinal plastic strain at a strain rate of 2450 s^{-1} and different temperatures for samples C, D, and E.

The observations made from Figures 18 and 19 are consistent with the results presented in Table 2, where ductility of the specimens was seen to increase with increase in temperature. The ductility of samples E and C is seen to be highest and lowest, respectively, judging from the reduction in the height and increase in longitudinal plastic strain of each group of samples at different temperatures. The fracture surfaces of the specimens that were tested at a strain rate of 2450 s^{-1} and at different temperatures are presented in Figures 20–22.

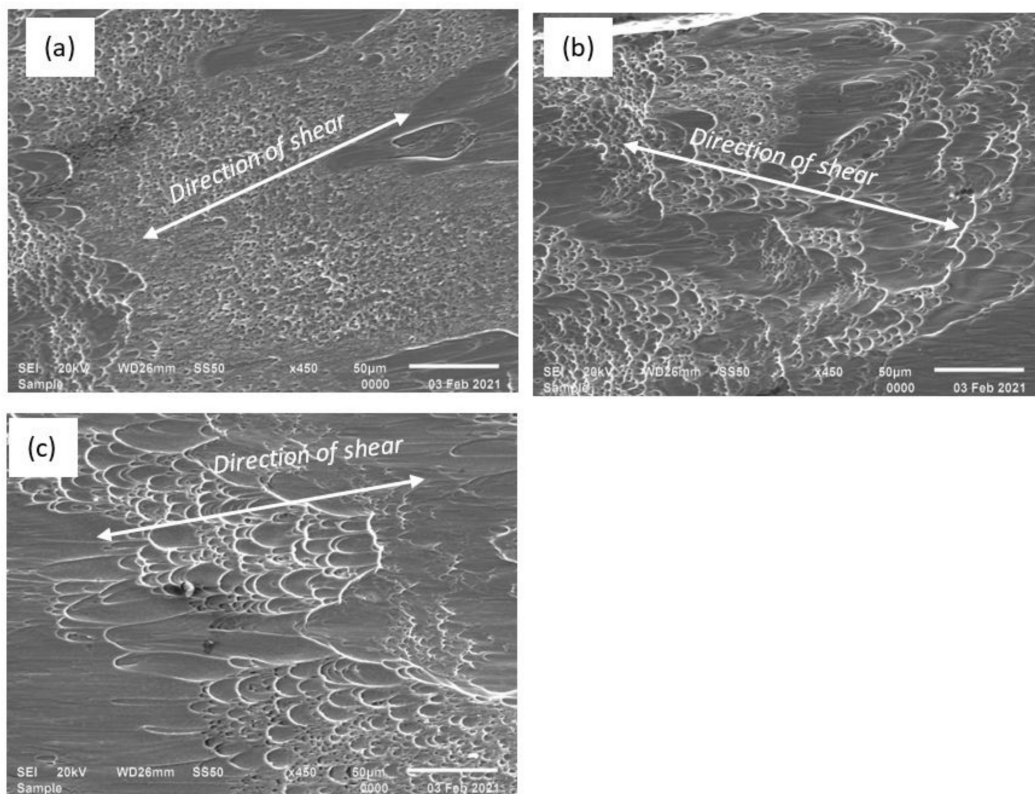


Figure 20. Typical characteristic features on the fracture surfaces of samples C at temperatures of (a) 25 °C, (b) 200 °C, and (c) 500 °C at a magnification of X450.

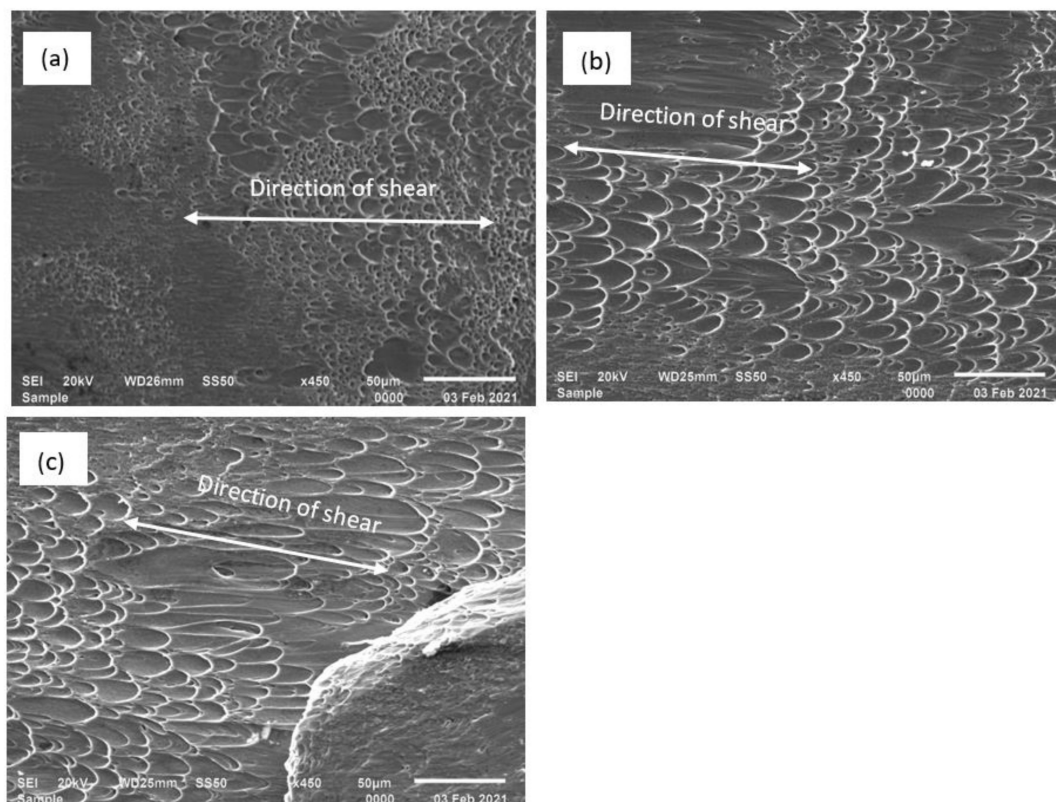


Figure 21. Typical characteristic features on the fracture surfaces of samples D at temperatures of (a) 25 °C, (b) 200 °C, and (c) 500 °C at a magnification of X450.

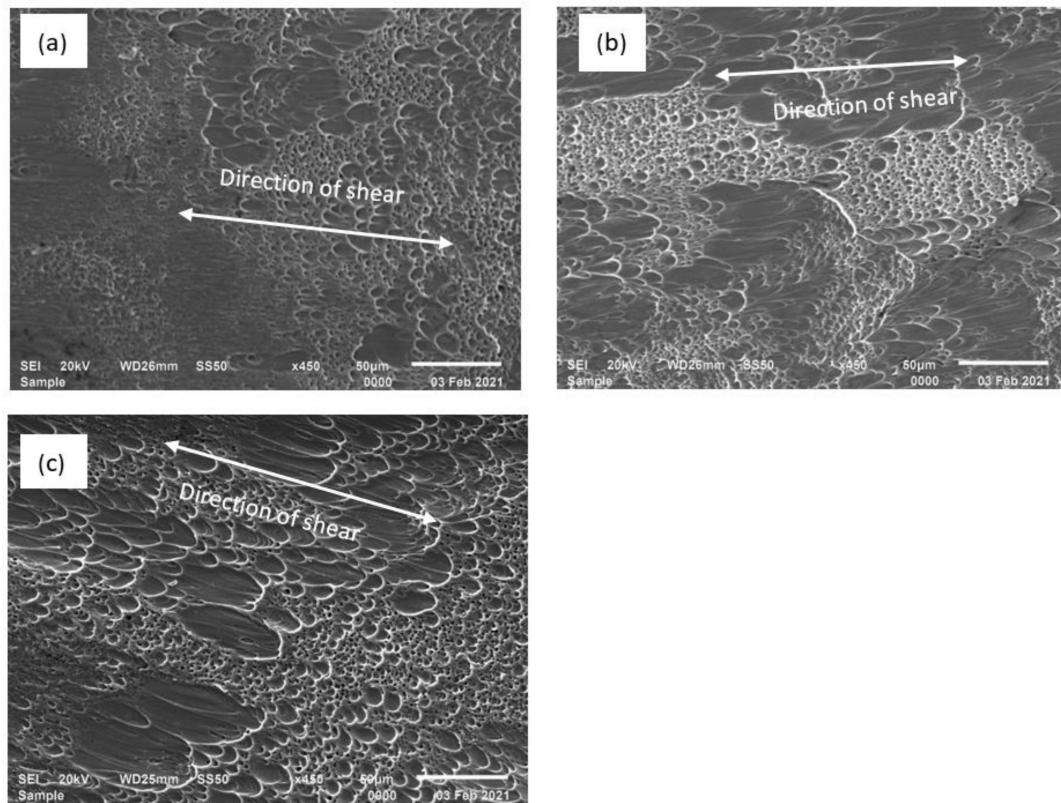


Figure 22. Typical characteristic features on the fracture surfaces of samples E at temperatures of (a) 25 °C, (b) 200 °C, and (c) 500 °C at a magnification of X450.

The micrographs of the fracture surfaces of samples C, D and E shown in Figures 20–22, respectively, show elongated dimples in all conditions of testing. The dimples are elongated along the directions of shear. These dimple features suggest that an array of microcracks/microvoids along the ASBs preceded the moment of fracture, with each microcrack/microvoid corresponding to a dimple. After dimples form from nucleated microvoids, their size increase with imposed flow stress, followed by their coalescence with other dimples to form larger dimples. This explains the multiple dimples of varying sizes on each fracture surfaces presented in Figures 20–22. The presence of dimples on a fracture surfaces denotes ductile fracture in contrast to smooth surfaces that are characteristic of cleavage, which is a sign of brittle fracture. It is interesting to note that in every case of the test samples here, the extent of elongation of these dimples was affected by the test temperature. At the temperatures of 200 and 500 °C the dimples are seen to be more elongated in comparison with ones resulting from the tests conducted at room temperature (25 °C). A summary of the major and the minor diagonal lengths of these dimples for different samples seen in Figures 20, 21 and 22 at different temperatures is presented in Table 5.

Table 5. The range of dimple lengths in different DMLS Ti6Al4V(ELI) samples fractured at a strain rate of 2450 s^{−1} and at different temperatures.

Temperature (°C)	25		200		500	
Alloy	Dimples Size Range (Major & Minor Diagonals) in (µm)					
	Major	Minor	Major	Minor	Major	Minor
Samples C	1–10	1–7	8–25	5–20	20–60	15–24
Samples D	3–15	3–10	12–30	8–20	25–60	15–25
Samples E	3–15	3–10	6–25	6–20	17–60	10–40

As seen in Table 5, both the major and minor diagonal lengths of dimples increase with increase in temperature for all cases of samples tested. This confirms that plastic deformation of the specimens increases with increased temperature and thus supports the inference of increased ductility with increasing temperature of the various microstructures of the DMLS Ti6Al4V(ELI) alloy tested here.

4. Conclusions

The three different microstructures of Ti6Al4V(ELI) produced by DMLS technology followed by heat treatment and their corresponding properties at high strain rate and temperature have been presented and discussed in this paper, with the following conclusions deduced:

- The DMLS Ti6Al4V(ELI) showed a wide range of microstructures dependent on heat treatment regime. The average α -lath thickness increased from 2.5 to 6 μm and 9 μm for heat treatment temperatures of 800, 940 and 1020 $^{\circ}\text{C}$, respectively.
- Samples C and D exhibited a random α -lath texture, however, some α -lath crystallographic orientations were repeated within the same prior β -grains. The colonies of α -lathes within the equiaxed and semi-equiaxed morphologies in samples E, consisted of crystals with a similar orientation.
- Samples C (heat treated at 800 $^{\circ}\text{C}$) recorded the highest value of Vickers microhardness. A decline in hardness was noted upon heat treatment at 940 $^{\circ}\text{C}$ for samples D which was attributed to coarsening of α -lathes. Surprisingly, a gain in hardness was then seen to occur in samples E that were heat treated just above the $\alpha \rightarrow \beta$ transformation temperature, even though these samples recorded a higher average size of the α -lathes.
- It was shown that the microstructures of samples C, D and E are sensitive to strain rate and temperature, with the flow stress increasing with increase in strain rate and decreasing with the increase in temperature.
- Samples C and E yielded at the highest and lowest value of stress at most of the test conditions, respectively. This was attributed to variation in microstructure where samples C with smaller grain sizes resulted in higher dynamic strength and samples E yielded at lower stress due to the presence of coarse α -lathes in the microstructure.
- The strain rate sensitivity of these samples varied, with samples D showing the highest value followed by samples E, while samples C showed the lowest values, at any given temperature. This difference was also ascribed to microstructure, in particular, the grain sizes and the texture.
- For all three different samples of DMLS Ti6Al4V(ELI), the deformation surfaces were characterised by the formation of ASBs running across the cut surfaces.
- The thickness of these ASBs increased with strain rate and temperature.
- The thickness of these ASBs also varied in different samples due to variation of hardness and strength of the samples as a result variation in heat treatment.
- Micrographs of the fracture surfaces of samples C, D and E were characterised by elongated dimples in all conditions of testing, and these dimples were elongated along the directions of shear, with their sizes increasing for deformation at high temperature.

Author Contributions: Conceptualization, A.M., M.M. and W.d.P.; methodology, A.M.; formal analysis, A.M.; writing—original draft preparation, A.M.; writing—review and editing, A.M., M.M. and W.d.P.; supervision, M.M. and W.d.P.; funding acquisition, W.d.P. All authors have read and agreed to the published version of the manuscript.

Funding: This research was funded by the South African Department of Science and Innovation (DSI) through the Council for Scientific and Industrial Research (CSIR), for the Collaborative Program in Additive Manufacturing, Contract No.: CSIR -NLC-CPAM-18-MOA-CUT-01.

Institutional Review Board Statement: Not applicable.

Informed Consent Statement: Not applicable.

Data Availability Statement: Not applicable.

Acknowledgments: The authors express their gratitude to the Centre for Rapid Prototyping and Manufacturing (CRPM) of the Central University of Technology, Free State (CUT), for production of the test specimens used for this study. The Centre for High Resolution Transmission Electron Microscopy (CHRTEM) of the Nelson Mandela University (NMU), where the EBSD analyses were carried out is acknowledged. The authors also acknowledge and thank Johan Westraadt of the CHRTEM for his commitment and technical assistance in interpretation of EBSD data. The Armaments Corporation of South Africa SOC Ltd. (ARMSCOR) where the SHPB experiments were conducted is also acknowledged. The department of Geology of the University of Free State is also acknowledged for providing the SEM for microstructural analysis.

Conflicts of Interest: The authors declare no conflict of interest.

References

1. Khaing, M.W.; Fuh, J.Y.; Lu, L. Direct metal laser sintering for rapid tooling: Processing and characterization of EOS parts. *J. Mater. Process. Technol.* **2001**, *113*, 267–272. [CrossRef]
2. Direct Metal Laser Sintering. Available online: <https://www.custompartnet.com/wu/direct-metal-laser-sintering> (accessed on 9 March 2021).
3. Uhlmann, E.; Kersting, R.; Klein, B.T.; Cruz, M.F.; Borille, A.V. Additive manufacturing of titanium alloy for aircraft components. *Procedia CIRP* **2015**, *35*, 55–60. [CrossRef]
4. Boyer, R.R.; Cotton, J.D.; Mohaghegh, M.; Schafrik, R.E. Materials considerations for aerospace applications. *MRS Bull.* **2015**, *40*, 1055–1065. [CrossRef]
5. Arcella, F.G.; Abbott, D.H.; House, M.A. Titanium alloy structures for airframe application by the laser forming process. In Proceedings of the AIAA-2000-1465, 41st Structures, Structural Dynamics, and Materials Conference and Exhibit, Atlanta, GA, USA, 3–6 April 2000.
6. Kobryn, P.A.; Ontko, N.R.; Perkins, L.P.; Tiley, J.S. Additive Manufacturing of Aerospace Alloys for Aircraft Structures. In Proceedings of the Cost-Effective Manufacture via Net-Shape Processing, Meeting Proceedings RTO-MP-AVT-139, Amsterdam, Netherlands, 15–19 May 2006; NATO: Neuilly-sur-Seine, France, 2006; pp. 3.1–3.14.
7. Riznyk, S.; Artushenko, A. Aero engine high pressure turbine blade cooling system concept. In Proceedings of the ASME Turbo Expo: Turbine Technical Conference and Exposition, San Antonio, TX, USA, 3–7 June 2013.
8. Vrancken, B.; Thijs, L.; Jean-Pierre, K.; Humbeeck, J. Heat treatment of Ti6Al4V produced by selective laser melting: Microstructure and mechanical properties. *J. Alloys Compd.* **2012**, *541*, 177–185. [CrossRef]
9. Khorasani, A.M.; Gibson, I.; Ghaderi, A.; Mahzer, I.M. Investigation on the effect of heat treatment and process parameters on the tensile behaviour of SLM Ti-6Al-4V parts. *Int. J. Adv. Manuf. Technol.* **2019**, *101*, 3183–3197. [CrossRef]
10. Teixeira, O.; Silva, J.G.; Ferreira, L.P.; Atzeni, E. A review of heat treatment on improving the quality and residual stresses of the Ti6Al4V parts produced by additive manufacturing. *Metals* **2020**, *10*, 1006. [CrossRef]
11. Millán, J.S.; Iñaki, A.; González, R. Strategies for static failure analysis on aerospace structures. In *Handbook of Materials Failure Analysis: With Case Studies from the Aerospace and Automotive Industries*; Salam, A., Makhoulouf, H., Mahmood, A., Eds.; Elsevier Ltd.: Cambridge, MA, USA, 2016; pp. 3–28.
12. Armendáriz, I.; Javier, Millán, S.; Olarrea, J. Strategies for dynamic failure analysis on aerospace structures. In *Handbook of Materials Failure Analysis: With Case Studies from the Aerospace and Automotive Industries*; Salam, A., Makhoulouf, H., Mahmood, A., Eds.; Elsevier Ltd.: Cambridge, MA, USA, 2016; pp. 29–55.
13. Shou-ngo, T. Dynamic loads in airplane structures during landing. *J. Aeronaut. Sci.* **1946**, *13*, 381–387.
14. Yu, X.; Cheng, L.; Chang, S.; Xuan, C.; Peiyuan, L. Foreign object damage performance and constitutive modelling of titanium alloy blade. *Int. J. Aerosp. Eng.* **2020**, 2739131. [CrossRef]
15. Sinha, S.K.; Dorbala, S. Dynamics loads in the fan containment structures of a turbofan engine. *J. Aerosp. Eng.* **2009**, *22*. [CrossRef]
16. Liu, L.; Zhao, Z.; Chen, W.; Luo, G. Ballistic impact behaviour of stiffened aluminum plates for gas turbine engine containment system. *Int. J. Crashworthiness* **2017**, *22*, 467–478. [CrossRef]
17. Durrenberger, L.; Molinari, A.; Rusinek, A. Internal variable modelling of the high strain-rate behaviour of metals with applications to multiphase steels. *Mater. Sci. Eng. A* **2008**, *478*, 297–304. [CrossRef]
18. Voyiadjis, G.Z.; Almasri, A.H. A physically based constitutive model for fcc metals with applications to dynamic hardness. *Mech. Mater.* **2008**, *40*, 549–563. [CrossRef]
19. Gray, G.T., III. High strain rate deformation: Mechanical behaviour and deformation substructures induced. *Annu. Rev. Mater. Res.* **2012**, *42*, 285–303. [CrossRef]
20. Peng-Hui, L.; Wei-Guo, G.; Wei-Dong, H.; Yu, S.; Xin, L.; Kang-Bo, Y. Thermomechanical response of 3D laser-deposited Ti-6Al-4V alloy over a wide range of strain rates and temperatures. *Mater. Sci. Eng. A* **2015**, *647*, 34–42.
21. Biswas, N.; Ding, J.L.; Balla, V.K.; Field, D.P.; Bandyopadhyay, A. Deformation and fracture behaviour of laser processed dense and porous Ti6Al4V alloy under static and dynamic loading. *Mater. Sci. Eng. A* **2012**, *549*, 213–221. [CrossRef]

22. Alaghmandfard, R.; Dharmendra, C.; Odeshi, A.G.; Mohammandi, M. Dynamic mechanical properties and failure characteristics of electron beam melted Ti6Al4V under high strain rate impact loadings. *Mater. Sci. Eng. A* **2020**, *793*, 139794. [[CrossRef](#)]
23. Fadida, R.; Shiriyzly, A.; Rittel, D. Dynamic tensile response of additively manufactured Ti6Al4V with embedded spherical pores. *J. Appl. Mech.* **2018**, *85*, 041004. [[CrossRef](#)]
24. Muiruri, A.; Maringa, M.; du Preez, W.; Masu, L. Effect of stress-relieving heat treatment on the high strain rate dynamic compressive properties of additively manufactured Ti6Al4V(ELI). *Metals* **2020**, *10*, 653. [[CrossRef](#)]
25. Muiruri, A.; Maringa, M.; du Preez, W.; Masu, L. Effects of stress-relieving heat treatment on impact toughness of direct metal laser sintering (DMLS) produced Ti6Al4V(ELI) parts. *JOM* **2020**, *72*, 1175–1185. [[CrossRef](#)]
26. Thejane, K.; Chikosha, S.; du Preez, W.B. Characterisation and monitoring of Ti6Al4V(ELI) powder used in different selective laser melting systems. *SAJIE* **2017**, *28*, 161–171. [[CrossRef](#)]
27. Els, J. Optimal Process Parameters for Direct Metal Laser Sintering of Ti6Al4V for Medical Implant Production. Master's Thesis, Department of Mechanical Engineering, Central University of Technology, Bloemfontein, Free State, South Africa, 2016.
28. Muiruri, A.; Maringa, M.; du Preez, W. Evaluation of Dislocation Densities in Various Microstructures of Additively Manufactured Ti6Al4V (ELI) by the Method of X-ray Diffraction. *Materials* **2020**, *13*, 5355. [[CrossRef](#)] [[PubMed](#)]
29. Song, B.; Chen, W. Energy for specimen deformation in a split Hopkinson pressure bar experiment. *Exp. Mech.* **2006**, *46*, 407–410. [[CrossRef](#)]
30. Gray, G.T. *Classic Split-Hopkinson Pressure Bar Testing*; ASM International: Materials Park, OH, USA, 2000; pp. 462–476.
31. Ramesh, K.T. High Rates and Impact Experiments. In *Handbook of Experimental Solid Mechanics*; Sharpe, W.N., Ed.; Springer: Boston, MA, USA, 2008; pp. 929–960.
32. Babu, B.; Lindgren, L.E. Dislocation density-based model for plastic deformation and globularization of Ti-6Al-4V. *Int. J. Plast.* **2013**, *50*, 94–108. [[CrossRef](#)]
33. Kocks, U.F. Realistic constitutive relations for metal plasticity. *Mater. Sci. Eng. A* **2001**, *317*, 181–187. [[CrossRef](#)]
34. Mecking, H.; Kocks, U. Kinetics of flow and strain-hardening. *Acta Metall.* **1981**, *29*, 1865–1875. [[CrossRef](#)]
35. Hull, D.; Bacon, D.J. *Introduction to Dislocations*, 5th ed.; Butterworth-Heinemann: Oxford, UK, 2011; pp. 53–57.
36. Conrands, H. Grain size dependence of the plastic deformation kinetics in Cu. *Mater. Sci. Eng. A* **2003**, *341*, 216–228.
37. Mao, Z.N.; An, X.N.; Liao, X.Z.; Wang, J.T. Opposite grain size dependence of strain rate sensitivity of copper at low vs. high strain rates. *Mater. Sci. Eng. A* **2018**, *738*, 430–438. [[CrossRef](#)]
38. Lesuer, D.R.; Kay, G.; LeBlanc, M. Modelling large-strain, high-rate deformation in metals. In Proceedings of the Third Biennial Tri-Laboratory Engineering Conference on Modelling and Simulation, Pleasanton, CA, USA, 3–5 November 1999.
39. Kocks, U. Laws for Work-Hardening and Low-Temperature Creep. *J. Eng. Mater. Technol.* **1976**, *98*, 76–85. [[CrossRef](#)]
40. Frost, H.J.; Ashby, M.F. Deformation-mechanism maps. In *The Plasticity and Creep of Metals and Ceramics*; Pergamon Press: Oxford, UK, 1982; pp. 134–147.
41. Taylor, G.I. Plastic strain in metals. *J. Inst. Metals* **1938**, *62*, 307–324.
42. Burger, W.G. On process of transition of cubic-body-centered modification into the hexagonal-close-packed modification of zirconium. *Physica* **1943**, 561–586. [[CrossRef](#)]
43. Chen, J.; Zhao, Y.; Yang, H.; Hiu, L.; Hong, Q. Investigation of adiabatic shear bands of Ti-B19 titanium alloy, Ti 2007: Science and technology. In Proceedings of the 11th World Conference on Titanium, Kyoto International Conference Centre, Kyoto, Japan, 3–7 June 2007.
44. Dodd, B.; Bai, Y. *Adiabatic Shear Localization—Frontiers and Advances*, 2nd ed.; Elsevier: Amsterdam, The Netherlands, 2012; pp. 183–200.
45. Xue, Q.; Meyers, M.A.; Nesterenko, V.F. Self-organization of shear bands in titanium and Ti6Al4V alloy. *Act Mater.* **2002**, *50*, 575–596. [[CrossRef](#)]
46. Lee, W.; Lin, C. Adiabatic Shear Fracture of Titanium Alloy Subjected to High Strain Rate and high Temperature Loadings. *J. de Phys. IV Colloq.* **1997**, *7*, 855–860. [[CrossRef](#)]